ACS APPLIED MATERIALS & INTERFACES

www.acsami.org

Research Article

Mesoporous Single Atom-Cluster Fe−N/C Oxygen Evolution Electrocatalysts Synthesized with Bottlebrush Block Copolymer-Templated Rapid Thermal Annealing

Dipankar Saha,[†] Hsin-Jung Yu,[†] Jiacheng Wang, Prateek, Xiaobo Chen, Chaoyun Tang, Claire Senger, James Nicolas Pagaduan, Reika Katsumata, Kenneth R. Carter, Guangwen Zhou, Peng Bai, Nianqiang Wu,* and James J. Watkins*

Cite This: *ACS Appl. Mater. Interfaces* 2024, 16, 13729−13744

Read Online

ACCESS | Metrics & More | Article Recommendations | Supporting Information

ABSTRACT: Current electrocatalysts for oxygen evolution reaction (OER) are either expensive (such as IrO_2, RuO_2) or/and exhibit high overpotential as well as sluggish kinetics. This article reports mesoporous earth-abundant iron (Fe)−nitrogen (N) doped carbon electrocatalysts with iron clusters and closely surrounding Fe−N_4 active sites. Unique to this work is that the mechanically stable mesoporous carbon-matrix structure (79 nm in pore size) with well-dispersed nitrogen-coordinated Fe single atom-cluster is synthesized via rapid thermal annealing (RTA) within only minutes using a self-assembled bottlebrush block copolymer (BBCP) melamine−formaldehyde resin composite template. The resulting porous structure and domain size can be tuned with the degree of polymerization of the BBCP backbone, which increases the electrochemically active surface area and improves electron transfer and mass transport for an effective OER process. The optimized electrocatalyst shows a required potential of 1.48 V (versus RHE) to obtain the current density of 10 mA/cm^2 in 1 M KOH aqueous electrolyte and a small Tafel slope of 55 mV/decade at a given overpotential of 250 mV, which is significantly lower than recently reported earth-abundant electrocatalysts. Importantly, the Fe single-atom nitrogen coordination environment facilitates the surface reconstruction into a highly active oxyhydroxide under OER conditions, as revealed by X-ray photoelectron spectroscopy and *in situ* Raman spectroscopy, while the atomic clusters boost the single atoms reactive sites to prevent demetalation during the OER process. Density functional theory (DFT) calculations support that the iron nitrogen environment and reconstructed oxyhydroxides are electrocatalytically active sites as the kinetics barrier is largely reduced. This work has opened a new avenue for simple, rapid synthesis of inexpensive, earth-abundant, tailorable, mechanically stable, mesoporous carbon-coordinated single-atom electrocatalysts that can be used for renewable energy production.

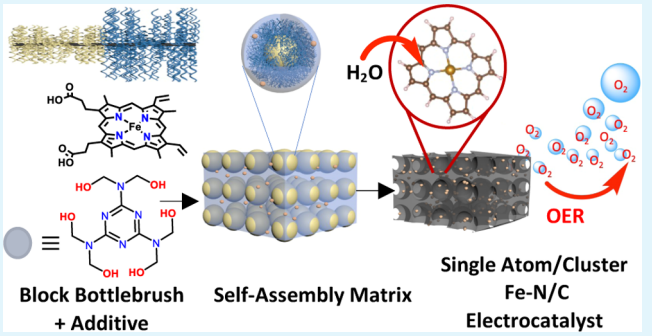

KEYWORDS: *electrocatalysis, carbon, oxygen evolution reaction, bottlebrush block copolymer, single-atom, in situ Raman spectroscopy, rapid thermal annealing*

INTRODUCTION

Hydrogen is an alternative energy source produced massively through water splitting and used as fuel with zero carbon dioxide emissions.[1−3] The electrochemical process involving water splitting often involves hydrogen production, accompanied by an oxygen evolution reaction (OER).[4−6] The OER involves a complicated four-electron process featuring proton-coupled electron transfer and strong oxygen−oxygen bonding,[7] leading to sluggish kinetics and a large energy barrier for water splitting. The state-of-the-art OER electrocatalysts typically contain very expensive platinum group metals (PGMs). Therefore, there is an urgent need to develop an inexpensive, high-performance electrocatalyst for efficient OER.

Transition metal (M)-based single atoms (SAs) with M−N/C moieties embedded in nitrogen (N)-doped carbonaceous scaffolds are emerging as an alternative to noble metal catalysts for various energy applications.[8,9] These materials exhibit the properties of both homogeneous and heterogeneous catalysts. M−N−C catalysts may contain multiscale metal phases from SAs and atomic clusters (ACs) to nanoparticles (NPs),

Received: December 15, 2023
Revised: February 28, 2024
Accepted: February 29, 2024
Published: March 8, 2024

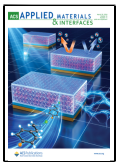

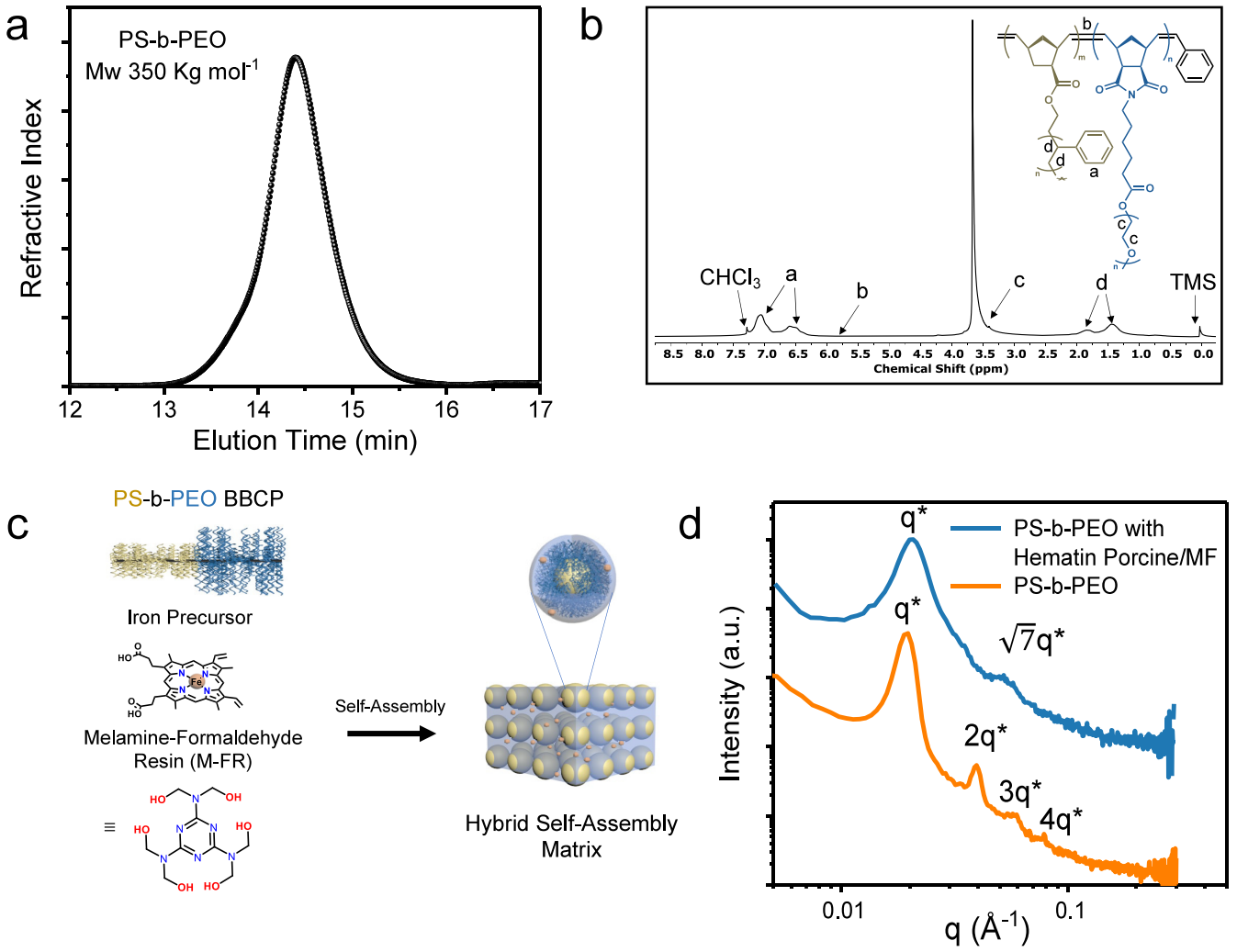

Figure 1. Characterization of iron–nitrogen bottle brush block copolymer composite. (a) GPC curve of the BBCP PS-*b*-PEO eluting in THF. (b) ^{1}H NMR spectrum of polymerized BBCP PS-*b*-PEO in $CDCl_3$ (500 MHz). Protons of interest are labeled. The PS peak (labeled as "a") is calculated after subtracting the chloroform peak. TMS (tetramethylsilane) is used as a reference of 0 ppm. (c) Schematic representation of self-assembly of PS-*b*-PEO BBCP, iron precursor, and M-FR to a hybrid matrix. (d) Room-temperature SAXS profiles of PS-*b*-PEO before and after blending with melamine–formaldehyde.

depending on the metal contents and the synthetic methods. Recent studies have shown that the electronic interactions between SA active sites and metal NPs/ACs can enhance the activity of single-atom catalysts (SACs) by unblocking the electron transfer pathways and very short interacting distances between SA active sites and metal NPs/ACs. By coordinating nitrogen dopant species with the active metal sites, the decreased surface energy prevents metal agglomeration, leverages local coordination, and enhances electrocatalytic performance. For example, cobalt(II) in silica-templated porous carbon has an overpotential of 320 mV at 10 mA/cm^2 current density for OER in 1 M KOH electrolyte,[10] while N-doped carbon materials with single-atom nickel sites showed good electrocatalytic activity for CO_2 reduction (current density of −4.2 mA/cm^2 at an overpotential of −0.76 V in 0.1 M $KHCO_3$ electrolyte).[8] A necessary characteristic for high performance was the large electrochemical surface area associated with the carbon materials. However, most of the reported porous carbon electrocatalysts involve a complicated synthesis process (such as a sol–gel hydrothermal process), following long pyrolysis (minimum of 10 h) to obtain a carbon skeleton for enhanced conductivity and electrocatalytic performance,[11,12] or employ expensive, low-yielding metal–organic frameworks (MOFs). These processes are not practical for large-scale production. Such limitations motivate the exploration of an easy, rapid, scalable approach to synthesize porous carbon-supported single metal atom materials for electrocatalytic applications.

It is worth noting that rapid thermal annealing (RTA) has been used as a simple and efficient way to produce porous structures within a minute time scale compared to conventional fabrication processes.[13] RTA is traditionally used in the semiconductor industry for doping, chemical modification, lattice damage repair, porosity modification, and graphene production.[14] Temperatures up to 1000 °C can be accessed via RTA within seconds in a desired gaseous environment at a rapid ramp rate (up to ∼150 °C/s).[15] Despite several advantages, RTA-based research for preparing mesoporous carbonized films for energy applications is still in its infancy.[16]

On the other hand, bottlebrush block copolymers (BBCPs) have drawn attention to synthesizing ordered porous carbon with tunable pore sizes (100 nm or larger) and well-ordered

https://doi.org/10.1021/acsami.3c18693
ACS Appl. Mater. Interfaces 2024, 16, 13729−13744

morphologies with bimodal pore size distributions.[17,18] BBCPs represent an emerging class of comb-like branched distinct macromolecules with densely grafted polymeric side chains on a polymeric backbone. Their rapid self-assembly has enabled fast preparation due to reduced entanglement, which simultaneously increases the accessible pore sizes of the templated material compared to the conventional methods that involve small surfactants. For example, we previously demonstrated that amphiphilic polydimethylsiloxane-*block*-poly(ethylene oxide) (PDMS-*b*-PEO) BBCPs with various molecular weights can be used as soft templates for porous carbons with spherical domain sizes ranging from 18 to 150 nm.[18] Similarly, we utilized PDMS-*b*-PEO BBCPs and polystyrene-*block*-poly(ethylene oxide) (PS-*b*-PEO) BBCPs as templates to concurrently generate 100 and 5 nm spherical domains via hydrogen bond-induced assembly with phenol-formaldehyde resin.[19] These polymeric systems have wide applications in gene therapy,[20] nanotemplating,[21] catalysis,[22] and energy storage.[16,23] BBCP templates enable precise tuning of the pore size of inexpensive carbon materials to design an electrocatalyst for producing renewable fuels.

Herein, we conceive an inexpensive, robust, scalable, and efficient approach for synthesizing mesoporous nitrogen-doped carbon material coordinated with single-atom and atomic iron clusters using RTA combined with a polystyrene-*block*-poly(ethylene oxide) (PS-*b*-PEO) BBCP as a soft template. Nitrogen-containing melamine-formaldehyde resin oligomers (M-FR) are used as carbon and nitrogen precursors. Iron incorporation enables the functionalization of the porous carbon. The single atoms and clusters of iron with N serve as the reactive centers for OER, whereas the atomic clusters support the single atoms to avoid demetalation during the OER process. Compared to other metals, the use of iron-based materials addresses the issues related to cost and scalability. The hybrid material is pyrolyzed using RTA to yield a robust iron−nitrogen carbon catalyst within 15 min. RTA facilitates carbonization in a few minutes without destabilizing the porous structure, which is characterized by high electrochemical surface area, uniform porosity, and good conductivity. XPS and *in situ* Raman spectroelectrochemistry studies are performed to gain insights into the mechanism of enhancement in OER reaction, revealing the emergence of electrocatalytically active oxyhydroxide at iron nitrogen coordination environment at a lower overpotential (250 mV) during the surface-reconstruction process. Finally, density functional theory (DFT) calculations substantiate that the reconstructed surface plays a pivotal role as the active site for an electrocatalytic reaction. A combination of rapid thermal and BBCP offers a general approach for the synthesis of a wide spectrum of porous carbon materials, which will find applications in electrocatalysis, photocatalysis, and solar-energy conversion and electrochemical energy storage.

RESULTS AND DISCUSSION

Additive-Driven Assembly of Brush Block Copolymer Composites. The PS-*b*-PEO BBCPs consisted of PS and PEO side chains with a molecular weight (M_w) of 5 kg mol^{-1}, a total molecular weight of 350 kg mol^{-1}, and a PS volume fraction (f) of 50% (Figure 1a). Their molecular weight was measured by gel permeation chromatography (GPC), and the chemical structure was confirmed by ^{1}H nuclear magnetic resonance (NMR) spectroscopy (Figure 1b). Further, to understand the morphological transition of PS-*b*-PEO BBCPs, small-angle X-ray scattering (SAXS) was carried out at room temperature. Neat PS-*b*-PEO BBCP was annealed at 110 °C to induce self-assembly before SAXS measurement. The SAXS profile revealed a strong secondary peak with a ratio of q*:2q*:3q*:4q*, indicating a lamellar morphology driven by the semirigid nature of molecular brushes (Figure 1c).

The concept of additive-driven assembly of block copolymers using selective hydrogen bonding to one block of a brush copolymer (such as with a PEO block) is well established.[18,24,25] Herein, hematin porcine was infused with melamine−formaldehyde (M-FR) resin into the BBCPs which exhibits strong hydrogen-bonding interactions with the PEO domain. The thin film was prepared by rod coating following thermal annealing to initiate cross-linking of M-FR. Spherical morphologies were formed via self-assembly during solvent evaporation, with PS appearing as the spheres and hematin porcine/M-FR-incorporated PEO domain as the matrix. M-FR resin was selected as a hydrogen bond donor for additive-driven assembly of the well-ordered precursor phase because M-FR selectively interacts with the PEO domain in PS-*b*-PEO BBCPs to enable the formation of well-ordered morphologies. Further, it can yield both nitrogen and carbon after carbonization, which is necessary to form a nitrogen-doped carbon structure. On the other hand, hematin porcine, a macrocyclic compound with a distribution of iron and nitrogen ($Fe-N_4$) supported by carbon, commonly used to obtain Fe−N/C electrocatalysts via pyrolysis, also formed hydrogen bonds with the PEO domain and M-FR. Hence, a mixture of PS-*b*-PEO and hematin porcine/M-FR was maintained in a mass ratio of 10:3. SAXS measurement was performed after blending PS-*b*-PEO with hematin porcine/M-FR and annealing at 70 °C for 15 min. As expected, strong microphase separation was observed after blending with hematin porcine/M-FR. It can be surmised that the selective hydrogen bonding of M-FR to PEO side chains leads to an increase of χ between PEO and PEO/hematin porcine/M-FR hybrid, enabling the formation of well-ordered morphologies. A scattering peak position ratio of q*:$\sqrt{7}$q* confirmed the formation of spherical morphologies (Figure 1b), where PS served as a minor domain. This ratio indicates that when the additive amount was added to PS-*b*-PEO BBCP, we observed an interesting order-to-order transition from lamellar to body center cubic (BCC) packing spherical morphology, as evidenced by the q* position ratio of 1:$\sqrt{7}$.[26] Thus, the use of BBCP templates resulted in the rapid formation of a spherical morphology with access to large domain sizes in the ordered precursor composite (Figure 1d), which exhibited fewer entanglements compared to their linear block copolymer counterparts. This means that PS-*b*-PEO BBCPs can be used as soft templates for hydrophilic precursors that establish strong hydrogen bonding with PEO side chains and eventually prepare porous functional materials.

Structural Analysis and Mechanistic Insight into the Nature of Fe−N Doped Porous Carbon. The synthesized BBCP was used as a sacrificial pore-forming agent and removed during pyrolysis.[27] Two stages of heating conditions were used to obtain the carbonized porous structure. The RTA process started with the partial degradation of PS-*b*-PEO BBCP at 250 °C accompanied by further heating to 800 °C to fully remove the BBCP templates to generate porous structures and carbonization of M-FR within 15 min (Figures 2a and S1). The elevated temperature is also crucial for the formation of optimal active sites and highly graphitic carbon support. Since the RTA pyrolysis process is very rapid, it is expected to

https://doi.org/10.1021/acsami.3c18693
ACS Appl. Mater. Interfaces 2024, 16, 13729−13744

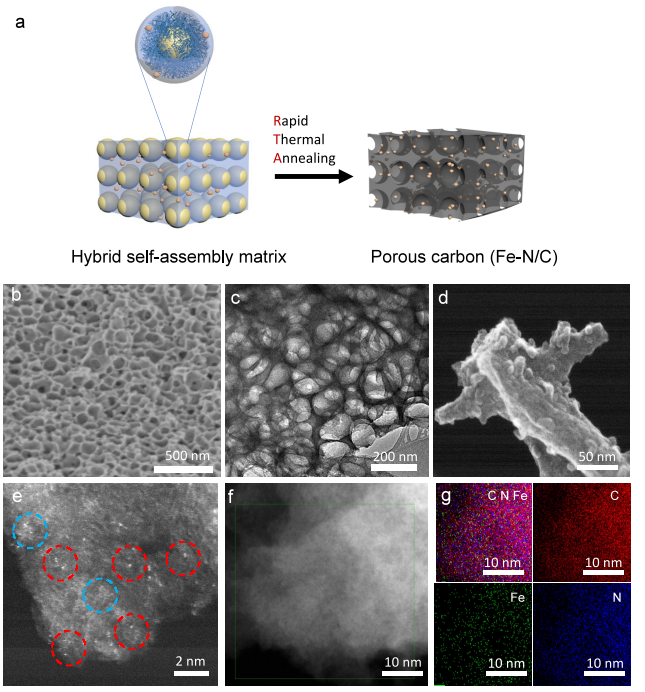

Figure 2. Morphological characterization of mesoporous Fe−N/C film: (a) schematic representation of RTA-induced transformation of self-assembled bottle brush block copolymer composite to mesoporous carbon; (b) SEM image; (c) TEM image; (d) HAADF-STEM image; (e) HAADF-STEM image with zoom-in image showing an iron cluster (blue circle) and its iron single atoms (red circles) distribution; (f, g) HAADF-STEM image and corresponding elemental mapping.

maintain the spherical pores upon heating. It is possible that metal clusters may be formed during the RTA pyrolysis process as metal−organic coordinated structures lead to agglomeration upon heating but can be minimized the cluster formation using the RTA process due to the small duration of pyrolysis. Scanning electron microscopy (SEM) revealed a homogeneous porous carbon structure, which should ensure excellent conductivity of the material (Figure 2a). Pores of ∼79 nm in diameter were generated after RTA (Figures 2b,c and S2), indicating successful BBCP templating during the *in situ* preparation of Fe−N-porous carbon. The abundant mesopores in the carbonized samples were expected to facilitate mass transport during the OER process and host Fe−N. Atomic-resolution high-angle annular dark-field scanning transmission electron microscopy (HAADF-STEM) was performed to investigate the distribution of iron species at the atomic scale (Figure 2d−g). The coexistence of iron single atoms and single-layer atomic clusters was observed on the nitrogen-doped carbon support. The magnified image in Figures 2e and S3 can be confirmed (although not quantified) that several iron atoms (red circles) were closely surrounded by a cluster (blue circle) at a distance of 0.46 nm (Figure S4), indicating the construction of single-atom iron catalysts and clusters. It is important to note that the atomic cluster in the Fe−N/C material was not introduced purposely as it is quite difficult to control the cluster formation during our material synthesis. Hence the distributions of cluster and single atoms in our samples are very random. However, according to the literature, the formed atomic cluster in Fe−N/C is highly preferred as the distance between the cluster and a single atom is important to understand the intrinsic OER behavior on Fe

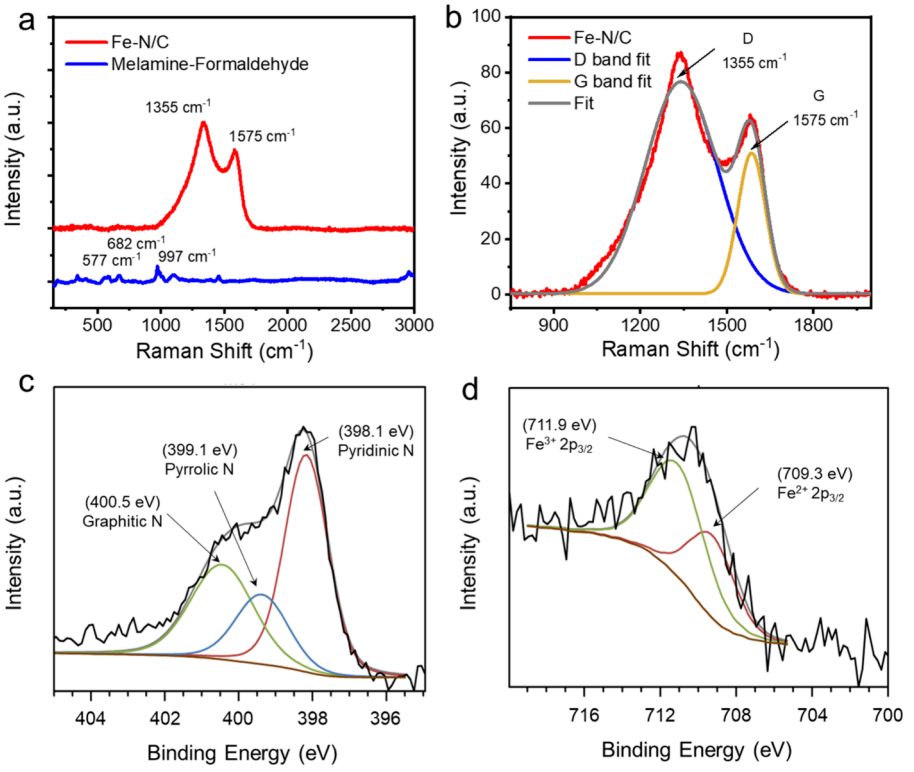

Figure 3. Spectroscopic characterization of mesoporous Fe−N/C film: (a) Raman spectroscopy of melamine−formaldehyde (blue curve) and carbonized films (red curve) at 633 nm; (b) deconvoluted Raman spectrum of D and G peaks showing the complete carbonization; high-resolution (c) N_{1s} and (d) Fe_{2p} XPS spectra of Fe−N/C film.

https://doi.org/10.1021/acsami.3c18693
ACS Appl. Mater. Interfaces 2024, 16, 13729−13744

atomic sites of the material.[28,29] The elemental maps display a uniform distribution of iron, nitrogen, and carbon throughout the samples without agglomeration of iron (Figure 2f,g). From HAADF-STEM images, we estimated (although not quantified) the average diameter of the iron atomic cluster to be ~0.54 nm (Figure S3) and the ratio of the single atom to the atomic cluster to be 5:1. It is possible that there was a fraction of single atoms far away from the atomic clusters that should behave like regular single-atom active sites. The Raman spectra of M-FR and carbonized Fe−N/C samples are shown in Figure 3a. The peaks at 577−682 cm^{-1} were attributed to ring bending and NH_2 symmetrical stretch vibrations of M-FR, respectively. The breathing mode of the triazine ring of M-FR was assigned to 997 cm^{-1}. These peaks were not observed in the carbonized Fe−N/C material. Instead, the peaks of the graphitic carbon-related G band (1575 cm^{-1}) and disordered D band (1355 cm^{-1}) indicate a substantial degree of carbonization (Figure 3b).[18,30] The significant intensity of the D band compared to the G band might have resulted from heavy nitrogen doping.[27] To understand the contribution of Fe incorporation in the carbon structure, an N-doped carbon sample (N/C) was prepared without Fe. The Fe−N/C (I_D/I_G = 1.34) and N/C samples (I_D/I_G = 1.32) had almost the same I_D/I_G ratio, suggesting a similar carbon network structure after incorporating Fe in the carbon moiety (Figure S5). This also implies that the degree of carbonization was controlled by the pyrolysis temperature regardless of the iron content. Further, Raman spectroscopy of the freshly prepared and five-week old Fe−N/C samples did not yield any significant differences in peak positions or intensities other than a slight increase of I_D/I_G ratio of 1.41, indicating that the synthesized Fe−N/C can be stable in the air for at least 35 days (Figure S6). The surface area and pore size distribution of Fe−N/C material were determined using adsorption/desorption isotherm with nitrogen as the adsorbing gas (Figure S7). It possessed a Brunauer−Emmett−Teller-specific surface area of 215 m^2/g. The surface area is comparable to that of the reported metal-based electrocatalysts.[11,31] The surface areas for Fe−N/C also imply that the Fesingle atoms were likely located in the pores, which may lead to a reduction in surface areas after Fe−N_4 hosting. Moreover, Fe−N/C material is enriched with mesopores of 79 nm, determined by SEM images with ImageJ software (Figure S2) which should enable the accessibility of the bulk of the material. Thus, the porous structure and surface area of synthesized Fe−N/C material ensures high electrocatalysis performance.

The carbonized Fe−N/C sample was further characterized using XRD (Figure S8). Iron carbide or nanocrystals were not detected in the XRD pattern, whereas an intense peak at $2\theta \sim 44°$ appeared in the carbonized iron sample without nitrogen (Fe−C) due to agglomeration of the iron nanoparticles.[32] However, a very weak peak at $2\theta \sim 44°$ for Fe−N/C agreed with our interpretation of HAADF-STEM analysis that nitrogen coordination with iron can prevent nanoparticle agglomeration. XPS helped us understand the composition and surface properties of Fe−N/C film (Figure 3c,d). The Fe−N/C sample was composed of 83 atom % carbon, 11 atom % nitrogen, and <1 atom % iron. The C 1s spectra revealed two different peaks at 284.5 and 285.5 eV, which correspond to graphitic (C═C) sp^2 and (C−C) sp^3 peaks, respectively (Figure S9).[8] This is consistent with the Raman data (Figure 3a,b). The Fe 2p core-level spectra exhibit peaks at 709.3 eV for Fe^{2+} $2p_{3/2}$ and at 722.7 eV for Fe^{2+} $2p_{1/2}$, as well as a satellite peak at 711.9 eV for Fe^{3+} $2p_{3/2}$ respectively (Figure 3d).[33] Notably, the Fe 2p spectrum shows the positively charged iron species without detecting any peak corresponding to metallic iron (706.0 eV)[33] in the Fe−N/C sample, indicating that single and clustered Fe atoms were possibly coordinated by the substrate N/C atoms. This supported the XRD data (Figure S8) and the HAADF-STEM image (Figure 2). The peaks at 398.1 and 400.5 eV of the high-resolution N 1s spectrum were assigned to pyridinic- and graphitic-N, while the corresponding peaks at 399.1 and 402.1 eV represent pyrrolic and oxidized nitrogen, respectively (Figure 3c).[34] The high pyridinic nitrogen content (43.8%) indicates that most of the N atoms in the carbon matrix were preferred to occupy at carbon defect or the edge sites.[33] Although XPS spectroscopy revealed the presence of nitrogen and iron species in the material, there was little direct evidence in the N 1s spectrum (binding energy ~399.0 eV) for coordination between iron and nitrogen atoms on Fe−N/C (Figure 3c).[8] Due to similar binding energies, it is difficult to deconvolute the XPS spectrum to distinguish between pyrrolic- and Fe−N coordinations.[35] Nevertheless, based on the XPS analysis and HAADF-STEM, it is reasonable to speculate that the introduction of Fe clusters is based on the utilization of protonated N-doped carbon substrate that has a moderate coordination strength to metal during heat treatment, thus achieving a balanced dispersion of iron single atoms and clusters. This may lead to the creation of Fe−N_4 hydride active sites during the OER process, following the transformation of the hybrid composite to mesoporous Fe−N/C material (Figure S2).

It is worth noting that the material characteristics from RTA were different from those obtained from conventional pyrolysis processes. Most methods for preparing porous carbon skeletons utilize SiO_2 nanoparticles or soft templates. These require high temperatures of >1000 °C for a minimum of 2 h with a slow ramp rate. Hence, the whole conventional pyrolysis process takes several hours. A control sample was calcinated in a nitrogen atmosphere in an oven at 800 °C for 8 h. SEM confirmed the formation of a porous structure templated by the PS-*b*-PEO BBCP (Figure S10). Also, XPS revealed that the nitrogen content was significantly reduced to ~5 atom % (Figure S11) because the long annealing process induced a higher degree of carbonization, which was consistent with the similar results reported.[36] On the other hand, the RTA process was leveraged to reduce the carbonization time drastically while maintaining the porous structure and the electrical conductivity of Fe−N/C film. The current vs. voltage plot was recorded using a two-probe system under ambient conditions. A current of 50 μA was measured at 0.8 V for the whole carbonized sample with a dimension of 1 × 1.5 cm (Figure S12).

Electrocatalytic Performance and Identification of Possible Active Sites. The electrocatalytic OER activity was tested using a nickel foam-supported Fe−N/C material as the working electrode in a typical three-electrode system with 1 M KOH aqueous electrolyte. Nickel foam (NF) is an ideal choice for nonself-supporting electrocatalysis materials to achieve practical application.[37] It possesses a three-dimensional open pore structure that supports the active electrocatalyst material due to its high surface area and rigid structure. First, the J-V curves were obtained, wherein a required potential to reach 10 mA/cm^2 of the porous Fe−N/C sample was determined to be 1.48 V (vs RHE) (Figure 4a). The Tafel slope is an important

https://doi.org/10.1021/acsami.3c18693
ACS Appl. Mater. Interfaces 2024, 16, 13729−13744

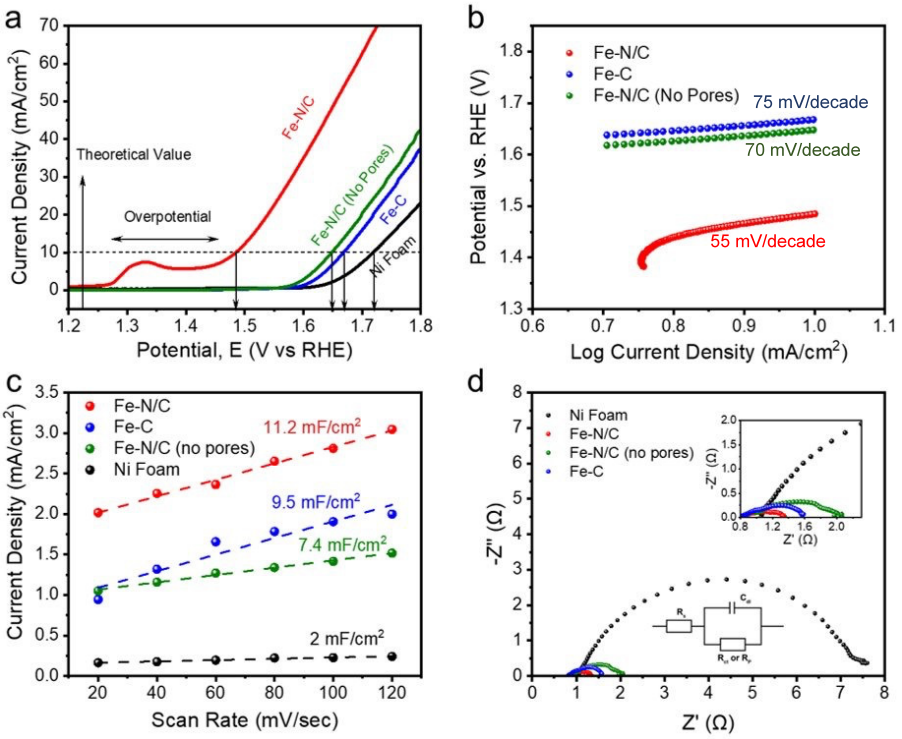

Figure 4. OER performance of synthesized catalysts. "Nickel foam" without any catalyst is used as a reference for comparison: (a) polarization graph of different catalysts in 1 M KOH electrolyte at a scan rate of 5 mV/s, where the surface area was normalized based on the geometric surface area; (b) corresponding Tafel plots, (c) electrochemical surface area, and (d) the Nyquist plot obtained from EIS at an applied DC potential of 0.35 V (Vs. RHE) in 1 M KOH electrolyte for Ni foam, Fe−N/C, Fe−N/C (no pores), and Fe−C, respectively. The inset shows the simulated equivalent circuit and zoom-in of the Nyquist plot.

parameter that provides insight into the electrocatalytic performance and mechanistic reaction pathway.[2] The Tafel equation can be written as eq 1:

$$\eta = a \log |\text{current density}| + b \quad (1)$$

where η, a, and b represent the overpotential, Tafel slope, and exchange current density, respectively. A linear fit of the Tafel equation provides the Tafel slope. A suitable electrocatalyst should have a lower value for the Tafel slope because a smaller slope represents a higher rate of oxygen production at a given overpotential.[1] A Tafel slope of 55 mV per decade was determined (Figure 4b) at an overpotential of 250 mV at a current density of 10 mA/cm^2 for Fe−N/C material (Figure 4a).

The OER rate is directly related to the electrochemically active sites on the catalyst surface. Various studies have reported that N coordination significantly enhances the overall electrocatalytic activity. Nitrogen coordination with metal plays an important role to stabilize the metal active sites in the catalyst to control the energetics of adsorption and desorption of the reaction intermediates by tuning the interactions between the metal atoms and the electronic structure of catalysts. Hence, linear sweep voltammetry (LSV) followed by Tafel slope calculation was performed on the control sample (carbonized PF/PSPEO/$FeCl_3$ (Fe−C) without nitrogen, SEM image shown in Figure S13) to determine the existence and impact of Fe−N active sites for OER. The J−V curve showed that the required potential to reach the current density of 10 mA/cm^2 of the Fe−C sample became 1.66 V (vs RHE) (Figure 4a). The overpotential increased by 180 mV. An increase in the Tafel slope from 55 (Fe−C) to 75 mV per decade (Figure 4b) suggested that the incorporation of N into the sample favored the OER process. On the other hand, an increase in the Tafel slope (Figure S14) of an N-doped carbon sample (N/C) without Fe further suggests a possibility of a synergistic effect between nitrogen and iron for the enhancement of the OER process. It is important to note that, a strong oxidative peak of Fe^{2+}/Fe^{3+} (1.25−1.35 V) is found in Figure 4a, which is prominent for porous Fe−N/C samples but absent in other samples including nickel foam, implying that the porous Fe−N/C samples can facilitate the oxidation and promote the OER process which is in line with the previous studies.[38] The pore size distribution of porous N-doped carbon electrocatalysts for OER is crucial due to the facile transport of electrolytes to the active sites. In electrocatalysts lacking a mesoporous structure, reactants and electrolytes struggle to reach the active sites within the catalyst particles. This limits OER participation to only the micropores on the particle surface. To demonstrate this point for our catalysts, we synthesized a small pore Fe−N/C electrocatalyst using a commercially available PS-*b*-PEO linear block copolymer using the same procedure that was used for PS-*b*-PEO BBCP and compared the performance with that of our prepared mesoporous Fe−N/C electrocatalyst to understand the pore size effect in the OER electrocatalysis process. The TEM images showed a pore size of 15 nm (Figure S15) with a homogeneous distribution of iron. The polarization graph showed a higher overpotential of 300 mV with a Tafel slope value of 65 mV/decade (Figure S16) compared to the BBCP-derived mesoporous Fe−N/C electrocatalyst. This result indicates that efficient mass transport during OER requires an interconnected large pore mesoporous structure to channel

https://doi.org/10.1021/acsami.3c18693
ACS Appl. Mater. Interfaces 2024, 16, 13729−13744

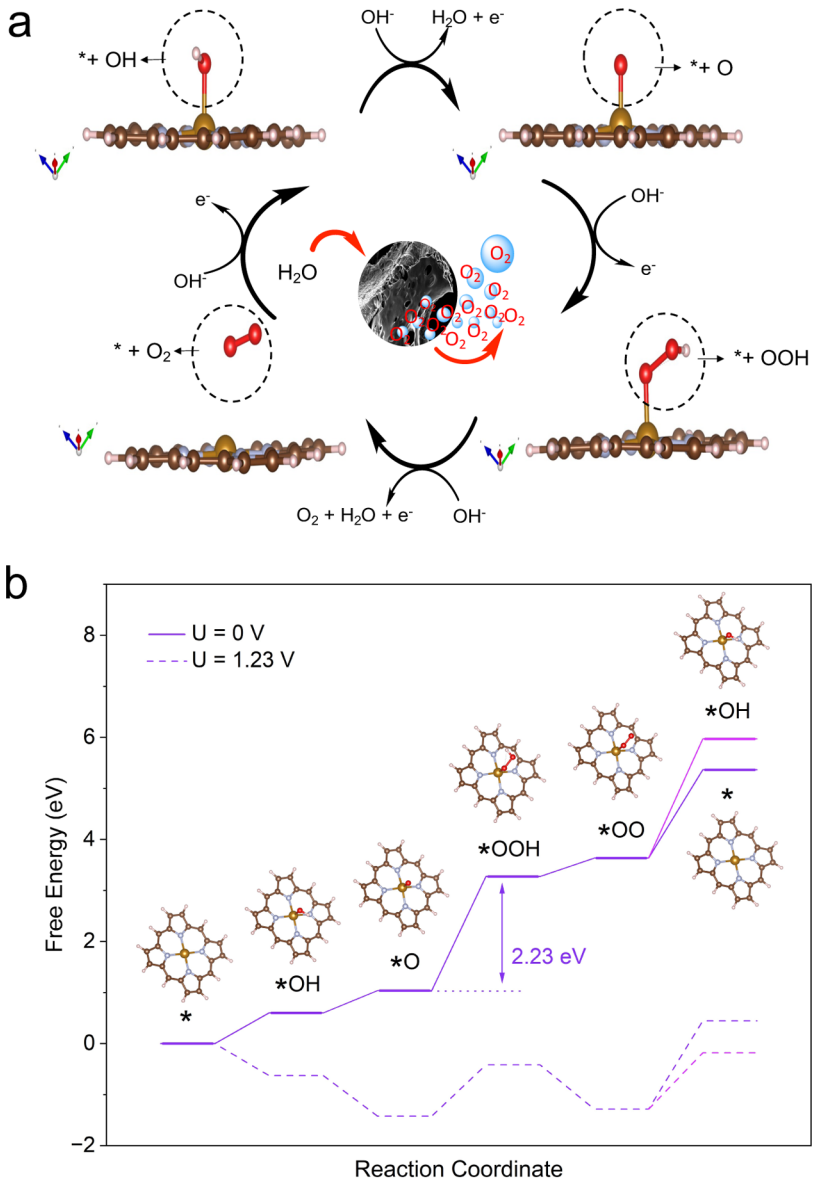

Figure 5. DFT calculations of the active site: (a) schematic illustration of the progress of the electrocatalytic OER process in Fe−N/C electrocatalyst; (b) schematic of the Gibbs free-energy changes on single atom Fe−N/C electrocatalyst at different applied potentials *U* for the four elementary steps during the OER based on DFT calculations.

reactants and electrolytes into the mesopores swiftly. Porous Fe−N/C electrocatalysts with 15 nm pore size lack this structure, and experience significantly reduced overall activity. Hence, controlling the pore size distribution is paramount for enhancing the performance of porous N-doped carbon electrocatalysts for OER. This phenomenon is also been observed in the reported studies.[39] The exceptional OER performance of our mesoporous Fe−N/C electrocatalyst is attributed to the interconnected mesoporous structure formed through our BBCP synthesis approach.

Further, to understand the influence of the conductive substrate (in this case Ni foam) in the OER performance, a glassy carbon electrode (GCE) was used as a conductive substrate for the control experiment. The mass loading of the catalyst (porous Fe−N/C) on GCE was the same as described for Ni foam support for the electrochemical performance. Unsurprisingly, an increase in polarization potential (corresponding overpotential 260 mV at 10 mA/cm^2 current density) was observed compared to the Ni foam support (Figure S17). Although this value is significantly lower than that of some reported electrocatalysts with Ni foam as conductive support.[40,41] Additionally, the Tafel slope value is also increased (62 mV/decade) compared to the Ni foam support porous Fe−N/C electrocatalyst which implies that Ni foam support can accelerate the oxygen production rate of porous Fe−N/C electrocatalyst and improve the OER activity of Fe−N/C electrocatalyst in line with reported studies.[37] The above results thus indicate that using NF as the substrate can be a highly efficient method for the practical application of nonself-supporting electrocatalyst materials.

It is essential to analyze the impact of the catalyst's porous structure on the electrocatalytic performance. Therefore, we prepared a nonporous control sample namely Fe−N/C without the incorporation of the BBCP template and measured the electrochemical performance using LSV. The nonporous structure was confirmed using high-resolution SEM (Figure

https://doi.org/10.1021/acsami.3c18693
ACS Appl. Mater. Interfaces 2024, 16, 13729−13744

S18). Unsurprisingly, the $J-V$ curve revealed that the required potential of the Fe−N/C sample (no mesopores) became 1.64 V to reach the current density of 10 mA/cm^2 (vs RHE) (Figure 4a). The overpotential increased by 160 mV. Also, a high Tafel slope of 70 mV per decade was observed, indicating that the mesoporous structure in Fe−N/C was essential to expose the active sites to the liquid electrolyte (Figure 4b) and facilitate the mass diffusion during the electrochemical OER process.[4] Meanwhile, the enhanced electrocatalytic performance may also be related to the improved electron transfer process between the electrocatalysts and the redox species in the electrolyte. Hence, electrochemical impedance spectroscopy (EIS) was carried out to study the electrode kinetics (Figure 4d). The Nyquist plot (Figure 4d) can be represented by the simulated equivalent circuit, as shown in the inset. The charge transfer resistance (R_{ct}) reflects the electron transfer between the electrocatalyst and the redox species in the electrolyte. The R_{ct} values were 10, 13, and 16 Ω for the porous Fe−N/C, porous Fe−C, and nonporous Fe−N/C samples, respectively. The R_{ct} value for porous Fe−N/C (10 Ω) is low compared to the benchmark values for Ir/C (54 Ω), and Pt/C (418 Ω), as supported by the polarization and Tafel results.[9,42] This result suggests that the pore structure and the N incorporated in the carbon matrix promoted electron transfer. The number of electrochemical active sites is reflected in the electrochemically active surface area (ECSA).[16,17] Hence, the double-layer capacitance (C_{dl}) and current density were measured at various scan rates for a given non-Faradaic potential window (0 to −0.3 V vs RHE) and then plotted and fitted linearly (Figure 4c). The capacitance value for Fe−N/C (11.2 mF/cm^2) is larger than those for Fe−C (9.5 mF/cm^2), nonporous Fe−N/C (7.4 mF/cm^2), and Ni foam (2 mF/cm^2). According to the literature, the electrochemical surface area is proportional to the C_{dl}, areas expressed by C_{dl}/C_s, where C_s is equal to 40 μF/cm^2 in alkaline aqueous electrolytes.[43−46] As a result, the electrochemically active surface area was estimated to be 280, 237.5, and 185 cm^2 for the porous Fe−N/C, porous Fe−C, and nonporous Fe−N/C samples, respectively. These results suggest that the surface iron species under a nitrogen environment exhibited intrinsic electrocatalytic activities for the reaction, which is consistent with the measured Tafel slope. The enhanced electrochemically active sites on the surface also indicate the accessibility and involvement of iron species as catalysts in the electrochemical process at the solid−liquid interface of the material.

Based on the above-mentioned results, the high OER performance of porous nitrogen-doped Fe−N/C material can be attributed to the following factors: (a) The short intersite distance facilitates the electron transfer from the iron atomic clusters to the iron single atoms that leads to higher electrochemical activity for OER, indicating that the cluster mainly acts as an activity booster. According to the previously reported literature, a distance of <1.6 nm between the Fe atomic cluster and a single atom helps reduce the overpotential, resulting from the weakened binding energy of *OH.[28,29] (b) The high electrochemically active surface area partly due to the Fe−N coordination environment increases the intrinsic activity of the catalyst which has also been reported to improve the OER process.[8,47] (c) Iron oxyhydroxide could form as a reconstructed surface during the OER process and improve electrochemical water oxidation performance, and (d) there is the efficient charge transfer from the electrode to the electrolyte due to iron incorporation, mesoporous structure, and the beneficial synergy with nickel foam.

The electrocatalyst developed in this work was compared with other Fe-, Ni-, or Co-based OER electrocatalysts reported previously (Table S1, Figure S19). Our catalyst had outstanding overpotential and Tafel values. In addition, it is worth noting that most of the reported metal N carbon/graphene-based electrocatalysts derived from multiple-step annealing of linear block copolymers, metal−organic frameworks (MOFs), and metal-implanted quantum dots are only explored for oxygen reduction reaction (ORR) and electrochemical CO_2 reduction reaction (CO_2RR).[9] One of the key findings of this work is that the N-coordinated iron single atom and atomic cluster electrocatalyst preparation uses a simple BBCP self-assembly with a single-step rapid annealing completed within minutes.

Mechanistic Insights into the Water Oxidation: First-Principle Calculations and Spectroscopic Verification. To understand the mechanism of the OER process on the electrocatalysts, DFT calculations were performed (Figures 5 and S20). According to the previously reported studies, it is experimentally demonstrated that the Fe atoms in the cluster alone play a less significant role for OER, hence only the N-coordinated single iron atoms were considered in our calculations.[28,48] This model is similar to one examined by Shang et al.[49] Compared with previous computational studies, we focus here on OER mechanisms in alkaline media and systematically examine both the redox and pH equilibria. These calculations used a large cluster model, which avoids the nontrivial correction schemes that complicate periodic DFT calculations with non-neutral simulation cells and allows us to study different oxidation states of the metal clusters. As shown in the DFT calculations in Figure S20, vertical arrows represent nonredox, chemical steps, while horizontal and diagonal arrows represent one-electron oxidation and coupled ion/electron transfer reactions, respectively, both with free energies converted to reduction potentials relative to RHE. As the experiments were conducted in an oxidizing environment, Fe may exist in different oxidation states. Figure S20 illustrates the potential states of reactants and key intermediates, allowing us to map out possible pathways with minimal potential barriers. For instance, the interconversion between initial Fe complexes, A1 and A2, is predicted to have an equilibrium reduction potential of 1.34 V (vs RHE). Under an applied potential of 1.48 V, the initial Fe complex is therefore expected to exist predominantly in the Fe(III) state (A2). Subsequent reactions are computed to be downhill in free energy until it reaches $[N_4Fe^{V}{=}O]^+$ (C4). The step C4 → D5 and is thus considered to be the potential-determining step. If instead, we consider the Fe (II) complex (A1) as the starting compound and follow the diagonal steps, the subsequent steps are similarly downhill in free energy until it reaches $[N_4Fe^{IV}{=}O]^0$ (C3). The next step can occur as C3 → C4 or C3 → D4, but both are predicted to have a rather positive reduction potential, at 1.84 and 2.23 V, respectively, indicating much more difficult transformations. With either initial Fe oxidation state, the potential-determining steps are the nucleophilic attack of water on the Fe oxo, which is more facile from a high valent Fe oxo species, consistent with previous literature reports[50−52] and the experimental observation in this work. At this point, we would like to note that these computed reaction energies are probably best viewed as evidence for plausible active-site configurations and reaction pathways, rather than values that should be

https://doi.org/10.1021/acsami.3c18693
ACS Appl. Mater. Interfaces 2024, 16, 13729−13744

quantitatively compared with experiments. Besides the consideration of a single representative active site, benchmark calculations of pK_a values and redox potentials would suggest a combined error up to ∼0.5 eV for the level of theory and implicit solvation treatment.[53−55] The M06-L meta-GGA functional used in our calculations is a reasonably reliable choice and has been shown to have lower errors than the PBE functional typically used in periodic DFT calculations (e.g., a mean unsigned error of 5.24 vs 7.58 kcal/mol for ligand dissociation energies in large cationic transition-metal complexes).[56] Following conventions, the DFT results were presented in Figure 5 (b) as free energy profiles at different applied voltages. At U = 0 V (depicted by the purple solid lines), step III (*O + OH^- → *OOH + e^-) has the highest free energy barrier of 2.23 eV, making it likely the RDS for the overall OER reaction, while O_2 desorption (step IV) has the second highest barrier. Compared to the OH^- assisted pathway (eq 6′), the unassisted pathway (eq 6) is more favorable with a barrier of 1.73 eV. As the applied voltage increases to U = 1.23 V (purple dashed lines), OH^- assisted desorption of O_2 becomes more favorable, with a barrier of 1.1 eV, while the barrier for step III decreases to 1 eV, making both steps similarly demanding.

To corroborate the DFT calculations, XPS studies were further performed. Figure 6 shows the XPS core-level spectra of Fe 2p, O 1s, C 1s, and N 1s before and after the OER electrocatalysis tests, which is necessary to understand the state of the active sites and the possible origin of the enhanced electrochemical performance. The high-resolution O 1s XPS spectra of the post-OER sample (0 h) depict an increase in the peak area of the O 1s spectra at 531.2 eV compared to pristine material (Figure S21, Table 1). The formation of a metal oxyhydroxides layer on the catalyst surface during the electrochemical testing could explain this observation.[4,11] After OER testing, XPS analysis showed that the peak for Fe 2p (Figure 6a,b) was slightly shifted to a higher binding energy. This was not surprising because Fe ions were initially coordinated with N. During electrocatalysis, Fe ions became coordinated with O besides N, as illustrated in Figure S20. Further, minimal changes in the atomic percentages of Fe and N in the post-OER sample (0 h) suggest (Table 1) that only a small surface region participated in the oxyhydroxide formation (Figure 6b,f). The N 1s spectrum (Figure 6f) illustrates a peak at 399.4 eV due to Fe−N coordination in the post OER.[57,58] Peaks corresponding to pyridinic nitrogen at 398.2 eV and graphitic nitrogen at 400.5 eV were also observed in the post-OER sample (0 h) similar to the pristine Fe−N/C sample (Figure 6f). The C 1s peak at a binding energy of 284.5 eV was assigned to sp^2 C═C, which indicates the retention of graphitic structure in the post-OER sample (0 h) (Figure 6d); and the C 1s peak at the binding energy of 286.0 eV was attributed to −C−O in the $-COO^-$ and/or −C−OH moieties (Figure 6d). The peak at 287.4 eV may correspond to C═O in the $-COO^-$ moiety.[59] It is noteworthy that the XPS spectra confirm that our samples do not contain any detectable amounts of Ni considering all the XPS measurements carried out on the Ni foam, implying nickel foam was not directly involved in electrochemical water oxidation other than improving the conductivity and the electrochemically active area of our electrocatalyst (Figure 4a).

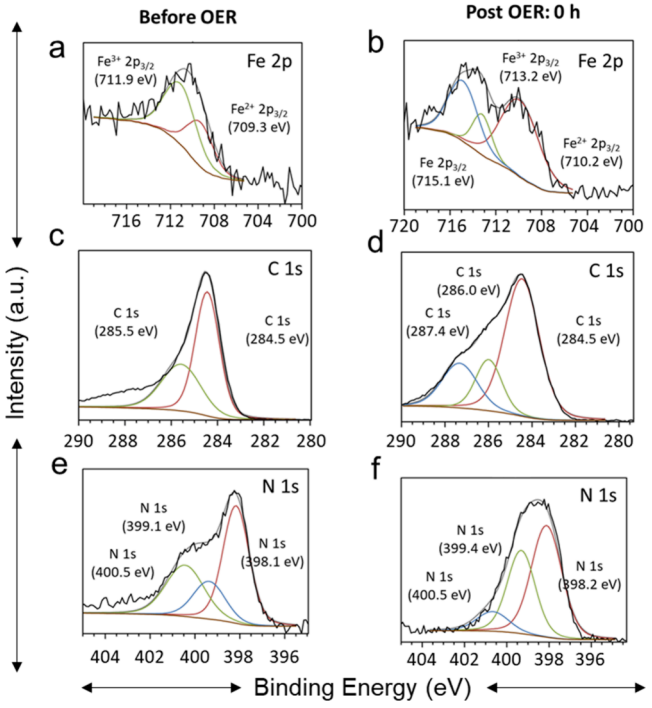

Figure 6. High-resolution XPS core-level spectra of the electrocatalyst. The left-hand and right-hand sides are the samples before (pristine sample) and after OER, respectively. Spectra are (a, b) Fe 2p, (c, d) C 1s, and (e, f) N 1s.

The real catalytic active sites may originate from the contribution of the iron−nitrogen coordinated with $-COO^-$ on the surface. Hence, based on the commonly recognized OER mechanism[4,60] our XPS and DFT results, the following reaction pathway was considered:

Step 1: Adsorption of Ions. The initial step requires the adsorption of OH^- ions onto the catalyst's active sites. The catalyst's active sites (denoted as *) further take OH^- ions as *OH by releasing an electron (eq 2):

$$\text{Active sites } (^*) + OH^- \rightarrow \text{Active sites } (^*)\text{-OH} + e^- \quad (2)$$

Step 2: Redox Reaction on the Catalyst Surface. In the second step, the active sites (*)-OH and OH^- present in the electrolyte participate in the redox reaction and form an oxide that adsorbed on the catalyst surface (eq 3).

$$\text{Active sites } (^*)\text{-OH} + OH^- \rightarrow \text{Active sites } (^*)\text{-O} + H_2O + e^- \quad (3)$$

Step 3: Formation of Molecular Oxygen. This step is comprised of two additional steps to form molecular oxygen

Table 1. Compositional Changes in the Fresh and Post-OER Samples from High-Resolution XPS

sample name	total C (atom %)	total Fe (atom %)	total O (atom %)	total N (atom %)	total Ni (atom %)
fresh (before OER)	82.8	0.7	5.6	10.9	
post-OER: 0 h	65.3	0.7	23.7	10.3	

https://doi.org/10.1021/acsami.3c18693
ACS Appl. Mater. Interfaces 2024, 16, 13729−13744

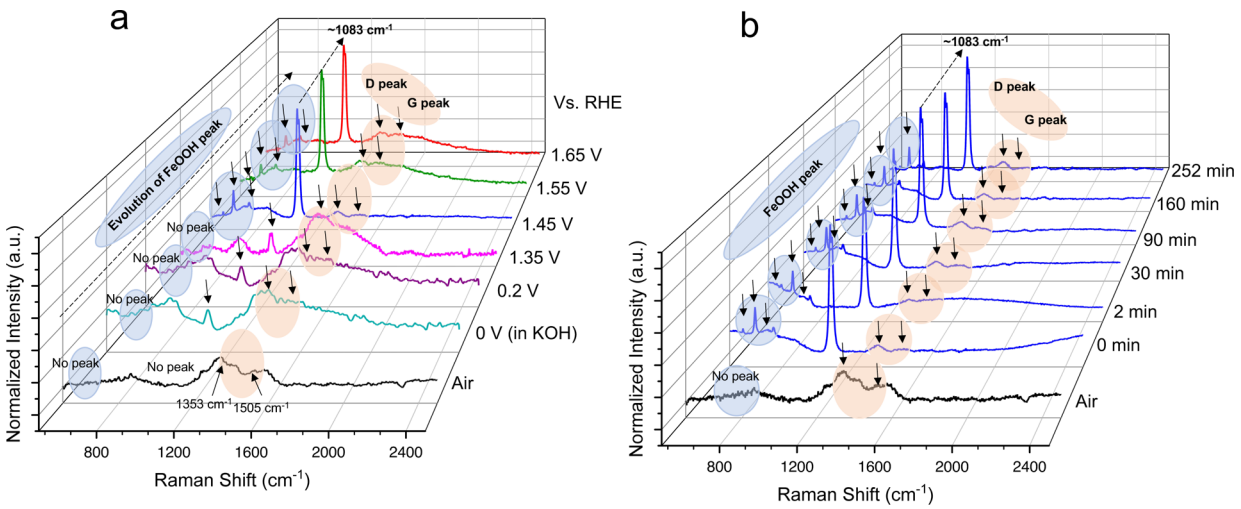

Figure 7. *In situ* Raman spectroscopy.: (a) *in situ* Raman spectra of Fe−N/C catalyst from air to 1.65 V vs RHE in 1.0 M KOH; (b) evolution of FeOOH on Fe−N/C over different time duration at 1.45 V vs RHE in 1.0 M KOH.

where the active sites (*)-O transform to active sites (*)-OOH, followed by the formation of dioxygen on the active sites (eqs 4 and 5).

$$\text{Active sites } (^*)\text{-O} + \text{OH}^- \rightarrow \text{Active sites } (^*)\text{-OOH} + \text{e}^- \quad (4)$$

$$\text{Active sites } (^*)\text{-OOH} + \text{OH}^- \rightarrow \text{Active sites } (^*)\text{-O}_2 + \text{H}_2\text{O} + \text{e}^- \quad (5)$$

Step 4: Desorption of Molecular Oxygen. The formed dioxygen leaves the catalyst surface at the end of the OER process via eq 6:

$$\text{Active sites } (^*)\text{-O}_2 \rightarrow \text{Active sites } (^*) + \text{O}_2 \uparrow \quad (6)$$

$$\text{Active sites } (^*)\text{-O}_2 + \text{OH}^- \rightarrow \text{Active sites } (^*)\text{-OH} + \text{O}_2 \uparrow + \text{e}^- \quad (6')$$

Briefly, iron-active sites are likely to accept the hydroxyl ions that boost the OER activity through discharging and desorption. The adsorption energy of H_2O is reported to be stronger on iron active sites than on any other metal sites. These sites eventually form oxygen−oxygen bonds by tuning the intermediate reaction species such as *OOH, *OH, or *O.[61] Our electrochemical measurements also suggest that the iron and nitrogen environment strongly influence the OER of Fe−N/C material. Step 3, the reaction from oxidation *O to *OOH, is considered as the rate-determining step, and the formation of *OOH is more favorable on Fe−N with N content, and without an N coordination in the Fe atom can lead to a higher Tafel slope consistent with previously reported results.[62] N can effectively reduce the aggregation size by decreasing the surface energy through more coordination with N, which is why a significant number of iron nanoparticles were observed under TEM.

To confirm the reaction pathway, especially the evolution of surface oxygen species, *in situ* Raman analysis was performed on the electrocatalyst during the chronoamperometry measurement in 1 M KOH electrolyte. Prior to electrocatalysis testing, two major peaks at ∼1346 and ∼1556 cm^{-1} of Fe−N/C (i.e., without immersion in KOH) can be assigned to the corresponding Raman-active bands of D and G (Figure 7a,b).[62] The graphitic characteristic D and G peaks of the Fe−N/C catalyst were quite low in intensity because the wavelength with photon energy does not match the optical band gap of the material, causing low enhancement of the Raman peaks.[63] A peak at around 1083 cm^{-1} may correspond to the amorphous nature of carbon that started emerging during the potential changes in the electrolyte and remains consistent throughout the OER process.[64] However, the absence of such a peak before immersing in the KOH solution indicated that the graphitic carbon structure might be disrupted during the OER process. Further, compared to the pristine states of Fe−N/C, there was a slight peak shift in the Fe−N/C electrode after being immersed in KOH (Figure 7a), which was due to the decreased laser power weakened by the electrolyte.[65] In the case of the Fe−N/C electrode under 1 M KOH with an applied potential of 1.45 V (vs RHE), Raman peaks appeared at ∼383, 421, 588, 651, and 757 cm^{-1}, which can be ascribed to FeOOH (Figure 7a and 7b).[66] This suggests that oxygen intermediates (i.e., *OH, *O, and *OOH) preferentially bind to Fe sites are closer to the N atoms, given that this elongates the bond length between the highly electropositive and electronegative elements and creates active sites with partial charges that are highly suitable for OER process.[67] A strong diffuse scattering from the aqueous electrolyte at low energies prevents any useful analysis of FeOOH peaks below ∼300 cm^{-1}. Our measurements suggest that the surface reconstruction into oxyhydroxide emerged at or above 1.35 V during the OER process and was stable up to 1.65 V (Figure 7a). Therefore, we believe that the main active species is FeOOH during the OER process, which agrees with the XPS and electrochemical test results when the potential was ≤1.35 V. Although with an increase in the applied voltage to 1.55 V vs RHE, the peak intensity at 420 cm^{-1} decreased, indicating that leaching out of some formed FeOOH occurred at a high applied potential. We also observed a shift in the peak position of 420 cm^{-1} in FeOOH when the applied bias was changed from 1.45 to 1.65 V (vs RHE). This was possibly due to Fe−N/C undergoing irradiation with a 785 nm laser (Figure 7a). An *in situ* measurement was carried out for 252 min at a constant potential of 1.45 V vs RHE to determine the surface reconstruction stability over time (Figure 7b). We did not observe any significant changes either in the Raman peak

https://doi.org/10.1021/acsami.3c18693
ACS Appl. Mater. Interfaces 2024, 16, 13729−13744

position or in the intensity, implying that the formed FeOOH was stable during the OER process and further supporting our XPS analysis. Thus, the DFT and spectroscopic results conclusively demonstrate that a single atom of Fe−N/C offered the highest intrinsic activity for OER, in agreement with the electrochemical test results.

One of the major challenges of iron single atom-based electrocatalysts is the degradation of materials over long periods of testing.[68] To identify this, we studied the durability of the OER electrocatalyst in 1 M KOH electrolyte using chronoamperometry (Figure S22a) and LSV measurements (Figure S22b,c). We found a steady and continuous current density up to 20 h. The OER activity of the post 20 h catalyst after the chronoamperometry test remains almost unchanged (Figure S22a). The high-resolution XPS showed no evident difference in the atomic percentage of oxygen between the post 0 and 20 h samples, while the presence of 399.9 eV of N 1s peak (Figure S23 and Table S2) further illustrates the existence of Fe−N coordination even after extended 20 h of OER operation. The peak at 398.7 eV corresponding to pyridinic nitrogen was also observed in the post 20 h OER sample, which was similar to the pristine and post 0 h OER samples. It is thus speculated that the enhanced stability of iron single atoms is due to the strong electronic interaction between Fe−N_4 and iron cluster because of unblocked electron transfer pathways and very short interacting distances, which lowers the tendency of the demetalation of Fe−N_4 sites. Additionally, the HAADF-STEM image of the used Fe−N/C catalyst after 20 h of chronoamperometry test (Figure S22d−-f) shows the well-retained single atom to atomic cluster, confirming its structural stability during the OER process. According to the literature, it is experimentally confirmed that the single Fe atoms, which only accounted for the Fe species in Fe−N/C, acted as the dominant reactive sites to form high-valence whereas, the atomic Fe clusters made up of the Fe species in Fe−N/C play only a minor role in the high-valence iron-oxo species. Therefore, the Fe single atom alone may have an excellent OER performance but will suffer the stability issue for long-term OER whereas the atomic Fe clusters alone cannot show a good OER activity because of lack of FeOOH formation during the process.[28,48] The absence of Ni peak in XPS spectra further confirms that our samples do not contain any detectable amounts of Ni in post 20 h OER. Thus, our results demonstrate that the synergy between single atoms and clusters is an effective strategy to improve the intrinsic activity and stability of single-atom active sites. SEM analysis of the post 20 h samples (Figure S24) after the chronoamperometry experiment indicated no evident change in the surface morphology of the electrocatalyst, even after the extended test. The stability of the mesoporous Fe−N/C electrocatalyst was also evaluated using cyclic voltammetry for 500 cycles (Figure S25) and no significant changes were detected in the OER electrochemical performance. This is consistent with our chronoamperometry experiment and electrochemical observation, which further demonstrate the robustness and stability of the electrocatalyst.

CONCLUSIONS

In summary, a rapid, energy-efficient, simple RTA approach was combined with the pyrolysis of polymer templates to generate mesoporous Fe−N/C electrocatalysts enriched with active sites containing single Fe atoms and clusters. Compared to conventional annealing methods, RTA permits the creation of porous carbon-based materials within only a few minutes. As a result, iron and nitrogen were distributed homogeneously in a porous structure with a pore size of ∼79 nm. The OER electrocatalytic activity of the Fe−N/C coating on Ni foam was evaluated. The electrocatalyst exhibited an overpotential of 250 mV and a Tafel slope of 55 mV/decade at a current density of 10 mA/cm^2 in 1 M KOH. The enhanced performance of the Fe−N/C electrocatalyst was attributed to the mesoporous structure, single atom sites, high electrochemical surface area, and high electrical conductivity. Creating a mesoporous structure and incorporating N and Fe into the carbon matrix with the Ni foam support increased the electrochemically active surface area, facilitating electron transfer and mass transport, lowering overpotential and Tafel slope. Importantly, a combination of *in situ* Raman spectroscopy and DFT calculations revealed the OER reaction mechanism and structure of the active phases. The Fe−N moiety served as the active site (*) for OER, and FeOOH was formed on the active site (*). Oxidation of *O to *OOH was considered as the rate-determining step in the OER reaction. This work has opened a path for synthesizing carbon-based electrocatalysts via BBCP-templated RTA. Beyond electrocatalysis, the extension of the devised synthetic protocol will also enable the fabrication of other metallic single-atom catalysts to facilitate other state-of-the-art reactions at the industrial scale. This approach can be adapted for various applications, including, but not limited to, electrocatalysis, electrochemical energy storage, sensors, and the development of sustainable technologies.

EXPERIMENTAL SECTION

Materials. *cis*-5-Norbornene-exo-2,3-dicarboxylic anhydride, *N*,*N*′-didcyclohexylcarbodiimide (DCC, >99%), 4-dimethylaminopyridine (DMAP, >99%), 5-norbornene-2-*endo*,3-exodicarboxylic acid (97%), ethyl vinyl ether (>99%), melamine (99%), formaldehyde solution (37 wt % in H_2O, contains 10−15% methanol as a stabilizer), hematin porcine (∼90%), magnesium sulfate (∼99.5%), ammonia solution (28−30%), anhydrous dimethylformamide (DMF, ∼99.8%), anhydrous dichloromethane (DCM, ∼99.8%), concentrated sulfuric acid (∼98%), and tetrahydrofuran (∼98%) were purchased from Sigma-Aldrich. Polymer Source provided the poly(ethylene glycol) monomethyl ether poly(styrene) (∼99%, Mw = 5 kg mol^{-1}) with a hydroxyl group and poly(styrene)-*b*-poly(ethylene oxide). Concentrated hydrochloric acid, methanol (∼95 wt %), and anhydrous ethanol were supplied from Fisher Scientific. Third-generation Grubb's catalyst (G3) was prepared based on the reported procedure.[69] Unless otherwise noted, all materials were used without further purification. Silicon wafers were purchased from University Wafer, Inc. (Boston, MA, USA). Ultrapure type I water (18.2 MΩ·cm) was used for all the experiments.

Synthesis of Polystyrene-*block*-Poly(ethylene oxide) Bottlebrush Block Copolymers (PS-*b*-PEO BBCPs). The norbornene-capped PS (PS-NB, Mw = 5 kg mol^{-1}) and PEO (PEO-NB, Mw = 5 kg mol^{-1}) macromonomers were synthesized according to a previous report.[18] To synthesize PS-NB macromonomer, the hydroxyl-terminated polystyrene (PS-OH) (2 g), *exo*-5-norbornenecarboxylic acid (0.27 g), *N*,*N*′-dicyclohexylcarbodiimide (DCC) (0.31 g), and 4-dimethylaminopyridine (DMAP) (0.03 g) were added into a dry flask followed by 50 mL of anhydrous DCM. The reaction was performed at room temperature for 3 days. After the reaction was finished, the product was condensed by rotary evaporation removing the excess solvent. The obtained concentrated mixture was then transferred to an extraction funnel along with 150 mL 1 M HCl and NaOH solution and collected the bottom part after three times extraction followed by a one-time brine solution. A substantial amount of magnesium sulfate was added to the obtained solution, stirred for 15 min, and filtered.

https://doi.org/10.1021/acsami.3c18693
ACS Appl. Mater. Interfaces 2024, 16, 13729−13744

The solid part was discarded and the excess solvent was removed by rotary evaporation to get a viscous solution. The obtained viscous solution was then precipitated dropwise in a chilled methanol solution and a white solid was collected as norbornene-terminated polystyrene (PS-NB) with Mw = 5 kg mol^{-1} (measured by GPC) after filtration and dried in a fume hood overnight. The PEO-NB was synthesized using a similar method and was purified in cold ether.

400 mg of each synthesized monomer (PEO-NB and PS-NB) was charged in the reaction vial with the desired amount of DCM under the Ar-filled glovebox. The concentrations for PS-NB and PEO-NB were 0.5 and 0.13 M, respectively. To initialize the ring-opening metathesis polymerization (ROMP), the PEO-NB was polymerized as the first block with a calculated amount of G3 catalyst for ∼15 min. After the completion of the PEO block, the second block PS-NB solution was added to the reaction mixture. The mixture was further reacted for additional 2 h to ensure complete polymerization, and the reaction was terminated with 0.2 g of ethyl vinyl ether. The ether-terminated reaction mixture was then dried overnight in a fume hood which yielded (∼100%) a light brownish solid as PS-*b*-PEO BBCP and was used without further purification.

Synthesis of Melamine-formaldehyde Resin. To prepare the melamine−formaldehyde resin (M-FR) oligomer, 1.26 g of melamine, 2 mL of formaldehyde solution (37 wt %), and 2 mL of ethanol were charged in a 20 mL reaction vial and stirred at 75 °C until the solution became clear with the formation of an M-FR oligomer. The solution was cool down to room temperature, added 25 μL of anhydrous triethylamine, and stirred for 0.5 h. After 0.5 h of stirring, the excess solvent was carefully removed by purging nitrogen until a transparent viscous solution was obtained (long nitrogen purging was avoided, otherwise a whitish condensed product can be formed).

Gel Permeation Chromatography. Gel permeation chromatography (GPC) of the brush block copolymers was conducted in THF containing 1.0 vol % triethylamine (TEA) on two PLgel 10 μm mixed-B LS columns in series with a multiangle laser light scattering (MALLS) detector and RI detector at a flow rate of 1.0 mL/min. Real-time d*n*/d*c* values were collected for each injection. Calibration standards were not necessary when assuming 100% mass elution from the columns.

Preparation of Iron−Nitrogen Bottlebrush Block Copolymer and Iron−Nitrogen Linear Block Copolymer Precursors. A 600 μL of PS-*b*-PEO solution (60 mg of synthesized PS-*b*-PEO was dissolved in 600 μL DMF) was mixed with 200 mg of M-FR prepolymer, and 140 μL of hematin porcine solution (96 mg of hematin porcine was dissolved in 2 mL of 2.8 vol % ammonia solution) was added to the above mixture. The solution was vortex mixed until a homogeneous solution was obtained. The mixture was rod-coated onto a silicon wafer of 10 μm thickness. After the solvent evaporation at room temperature, the precursors were annealed at 100 °C for 1 h under a vacuum to enable cross-linking and used for rapid temperature annealing treatment for the carbonization process.

For the preparation of iron−nitrogen linear block copolymer precursor, the same procedure was applied as described above but instead of using synthesized PS-*b*-PEO, a commercially available PS_{5k}-*b*-PEO_{5k} was used to obtain iron−nitrogen linear block copolymer precursor.

Preparation of Mesoporous Iron−Nitrogen Carbon Material. A Solaris 100 rapid thermal processing system in a nitrogen atmosphere was used to carry out the RTA process. Dried iron−nitrogen bottlebrush block copolymer and linear block copolymer precursor film separately onto a silicon wafer (for conductivity measurement) and nickel foam (for the electrochemical experiments) was calcinated at 250 °C with a ramp rate of 50 °C/s for 90 s, followed by 800 °C at a ramp rate of 10 °C/s for 3 min. Thus, the two-step process can ensure the complete degradation of BBCP and carbonization of the material. After complete carbonization, the sample was cooled down at room temperature in a nitrogen atmosphere, and a black solid was collected as a mesoporous iron−nitrogen carbon material for further experiments.

Conductivity Measurement. The conductivity of the material was measured using a chemiresistor geometry at room temperature with a two-probe Keithley 4200 semiconductor characterization system using a previously reported method.[70] Briefly, a 2 cm × 2 cm film (600 μL PS-*b*-PEO solution was mixed with 200 mg of M-FR prepolymer, and 140 μL of hematin porcine solution) was homogeneously spread onto a silicon oxide wafer and dried in an oven for 1 h at 160 °C under nitrogen environment. The metal contacts were prepared using two parallel conductive adhesive copper tapes attached 1 cm apart (channel dimension where the Fe−N/C material dried).

Surface Area Measurement and Pore Size Distribution. Nitrogen adsorption/desorption measurements were conducted on an Autosorb-1 system at 77 K after the sample was degassed at 150 °C for 24 h. The specific surface area was calculated using the Brunauer−Emmett−Teller (BET) method using the relative pressure from 0.1 to 0.2 with a positive C value for the calculation. It is important to note that the N_2 adsorption/desorption isotherm will not be able to determine the pore size distribution of over 50 nm ranges. Therefore, the SEM image with the help of ImageJ software (Figure S2) was used to estimate the pore size distribution of the Fe−N/C electrocatalyst.

Microscopy and Spectroscopy. Field emission scanning electron microscopy (SEM) measurements were carried out on FEI Magellan 400 FESEM at an accelerating voltage of 1 kV and a current of 25 pA. Transmission electron microscopy (TEM) measurements were performed using FEI/ThermoFisher Tecnai12 operated at an accelerating voltage of 200 kV. Scanning transmission electron microscopy (STEM) in high angle annular dark field (HAADF) imaging mode and energy dispersive X-ray spectrometry (EDS) were conducted using a Hitachi 2700C microscopy with a probe aberration-corrector and FEI Talos F200X microscopy equipped with a four-quadrant EDS detector at 200 kV accelerating voltage. X-ray diffraction (XRD) patterns were obtained with a Panalytical X-ray diffractometer with 1.5418 Å Cu Kα radiation. The ordered porous structure was characterized using a Ganesha SAXS-LAB small-angle X-ray scattering (SAXS) with 1.5418 Å Cu Kα radiation and an X-ray beam area of ∼0.04 mm^2. Bulk samples were prepared in a steel washer sealed by Kapton tape at elevated temperature, ensuring complete sealing with a thickness of 0.5 mm. The two-aperture systems were used for incident beam collimation. X-ray photoelectron (XPS) analysis was performed using a Physical Electronics VersaProbe III instrument equipped with a monochromatic Al Kα X-ray source ($h\nu$ = 1486.6 eV) and a concentric hemispherical analyzer. Charge neutralization was performed using both low-energy electrons (<5 eV) and argon ions. The binding energy axis was calibrated using sputter-cleaned Cu (Cu $2p_{3/2}$ = 932.6 eV, Cu $3p_{3/2}$ = 75.1 eV) and Au foils (Au $4f_{7/2}$ = 83.9 eV). Peaks were charged referenced to the sp^2 band in the carbon 1s spectra at 284.5 eV. Measurements were made at a takeoff angle of 45° w.r.t. the sample surface plane. These specifications resulted in a typical sampling depth of 3−6 nm (95% of the signal originated from this depth or shallower). Quantification was done using instrumental relative sensitivity factors (RSFs) that account for the X-ray cross-section and inelastic mean free path of the electrons. Major elements (>5 atom %) on homogeneous samples tend to have standard deviations of <3%, while minor elements can be significantly higher. The analysis size was ∼200 μm in diameter. CasaXPS software was used to analyze the spectra.

A DXR Raman microscope from Thermo Fisher Scientific was used for *ex situ* Raman spectrum over a range of 100−3500 cm^{-1} with a resolution of 5.3−8.8 cm^{-1}, using a 20× objective backscattering configuration. Three different spots of each sample were obtained using a focused 633 nm laser (power = 5 mW) on a 1.6 μm spot size to avoid sample damage. *In situ* Raman spectra were collected under controlled constant applied potential (vs RHE) using an electrochemical cell with a quartz window was used, consisting of a glassy carbon electrode as working electrode (Fe−N/C ink drop cast on a glassy carbon electrode with a working area of 3 mm × 3 mm) at the top, a Pt wire counter electrode, and an Ag/AgCl (saturated KCl) reference electrode. Raman spectra were acquired using a B&W Tek i-Raman Plus spectrometer under excitation by a focused 785 nm laser and a 20× objective backscattering configuration at 40% of the power. Fe−N/C ink was prepared using a mixture of 8% Nafion, 20%

https://doi.org/10.1021/acsami.3c18693
ACS Appl. Mater. Interfaces 2024, 16, 13729−13744

ethanol, and 80% water solution and probe sonicate (Qsonica sonicators) for 15 min at room temperature.

First-Principle Calculations. Density-functional theory calculations were performed using the Gaussian 16 software package, with the M06-L exchange-correlation functional and aug-cc-PVTZ basis set.[71−73] The mean unsigned error (MUE) for ligand dissociation energies in large cationic transition-metal complexes using the meta-GGA functional M06-L is 5.24 kcal/mol, which is much lower compared to classic GGA functional. The Stuttgart/Dresden effective core potential effective core potential ECP10MDF was used on Fe atoms,[74] and solvation effects were considered using the SMD model with water as the implicit solvent.[75] SCF cycles were converged to 10^{-8} Ha while geometry optimizations were stopped after maximum force, root-mean-square force, maximum displacement, and root-mean-square displacement dropped below 4.5×10^{-4} Ha/a_0, 3.0×10^{-4} Ha/a_0, 1.8×10^{-3} a_0, and 1.2×10^{-3} a_0, respectively. The reported reaction energetics correspond to the spin states with the lowest energies. The experimental solvation-free energies of H^+ in water were used for the calculation of standard reduction potentials (vs SHE) and converted to the RHE reference.[76]

Electrochemical Measurements and Electrode Preparation. A three-electrode configuration was used for all electrochemical measurements in a 1 M KOH for OER on a CH Instruments CHI660D electrochemical workstation at ambient temperature. Fe−N/C on nickel (Ni) foam support, graphite rod, and Ag/AgCl electrodes (saturated KCl) were used as working, counter, and reference electrodes, respectively. All the materials used for electrochemistry have been prepared as follows.

Ni foam (the active area is 2 cm^2, considering that the catalyst is coated on both sides of the foam) was pretreated in an HCl solution (2 M, 10 mL) for 15 min and washed with DI water. To prepare the working Fe−N/C electrode on Ni foam, pretreated Ni foam was immersed into the prepared iron−nitrogen bottle brush block copolymer precursor and, subsequently, taken out and dried in an oven at 100 °C under vacuum for an hour. This procedure was repeated at least three times until the catalyst loading reached 1 mg/cm^2, measured as accurately as possible using an analytical balance, and carbonized using RTA under the carbonized condition mentioned earlier. Three different precursors were first prepared to obtain three control samples on pretreated Ni foam. Precursor 1 was a melamine-formaldehyde resin (M-FR)/Fe precursor without PS-*b*-PEO BBCP, precursor 2 was a phenol-formaldehyde resin (P-FR)/PS-*b*-PEO/Fe precursor, and precursor 3 was an M-FR/PS-*b*-PEO precursor without hematin porcine solution. Then the pretreated Ni foam was immersed into those precursors and followed a similar procedure as mentioned above to obtain Fe−N/C with no pores, Fe−C with no nitrogen, and N/C with no iron electrode materials on Ni foam. A glassy carbon electrode (GCE, 0.071 cm^2) was used for the controlled experiment as the working electrode. Fe−N/C ink (3 mg) was prepared using a mixture of 8% Nafion, 20% ethanol, and 80% water solution and probe sonicate (Qsonica sonicators) for 15 min at room temperature. Five μL of the above ink was drop cast on the GCE until the mass loading 1 mg/cm^2, then dried to form the working electrodes. The morphological characterization of the electrocatalyst reported in this manuscript was performed through direct fabrication on nickel foams except for the conductivity measurement where silicon was used as a substrate.

Linear sweep voltammetry (LSV) with a sweep rate of 5 mV/s was carried out using a three-electrode system with 1 M KOH electrolyte. Cyclic voltammetry was carried out using the same three electrodes set up with a 10 mV/s scan rate. A long-term stability test for the current vs. time graph was carried out in a 1 M KOH electrolyte using a three-electrode system with a fixed overpotential. All the potentials reported in this work are adjusted with the reversible hydrogen electrode (RHE). The equilibrium potential (E_0) for OER is 1.23 V vs. RHE, so the potential difference between E_{RHE} and 1.23 V is the overpotential. Electrochemical impedance spectroscopy (EIS) was performed using a CH Instruments CHI660D electrochemical workstation at ambient temperature with frequencies in the range of 100 kHz to 10 Hz at a voltage amplitude of 10 mV. Each electrochemical experiment was run at least three times for reproducibility.

■ ASSOCIATED CONTENT

Supporting Information

The Supporting Information is available free of charge at https://pubs.acs.org/doi/10.1021/acsami.3c18693.

Experimental and computational details, additional SEM, TEM, and HAADF-STEM images, XPS data, Raman data, and additional analysis of the electrochemical data (PDF)

■ AUTHOR INFORMATION

Corresponding Authors

Nianqiang Wu − *Department of Chemical Engineering, University of Massachusetts Amherst, Amherst, Massachusetts 01003, United States;* orcid.org/0000-0002-8888-2444; Email: nianqiangwu@umass.edu

James J. Watkins − *Conte Center for Polymer Research, Department of Polymer Science and Engineering, University of Massachusetts Amherst, Amherst, Massachusetts 01003, United States;* orcid.org/0000-0001-8302-825X; Email: watkins@polysci.umass.edu

Authors

Dipankar Saha − *Conte Center for Polymer Research, Department of Polymer Science and Engineering, University of Massachusetts Amherst, Amherst, Massachusetts 01003, United States;* orcid.org/0000-0002-6268-2807

Hsin-Jung Yu − *Conte Center for Polymer Research, Department of Polymer Science and Engineering, University of Massachusetts Amherst, Amherst, Massachusetts 01003, United States*

Jiacheng Wang − *Department of Chemical Engineering, University of Massachusetts Amherst, Amherst, Massachusetts 01003, United States;* orcid.org/0000-0002-7948-8525

Prateek − *Conte Center for Polymer Research, Department of Polymer Science and Engineering, University of Massachusetts Amherst, Amherst, Massachusetts 01003, United States;* orcid.org/0000-0002-7305-5550

Xiaobo Chen − *Department of Materials Science and Engineering, Binghamton University, State University of New York at Binghamton, Binghamton, New York 13850, United States*

Chaoyun Tang − *Department of Chemical Engineering, University of Massachusetts Amherst, Amherst, Massachusetts 01003, United States*

Claire Senger − *Conte Center for Polymer Research, Department of Polymer Science and Engineering, University of Massachusetts Amherst, Amherst, Massachusetts 01003, United States*

James Nicolas Pagaduan − *Conte Center for Polymer Research, Department of Polymer Science and Engineering, University of Massachusetts Amherst, Amherst, Massachusetts 01003, United States;* orcid.org/0000-0001-6565-3553

Reika Katsumata − *Conte Center for Polymer Research, Department of Polymer Science and Engineering, University of Massachusetts Amherst, Amherst, Massachusetts 01003, United States;* orcid.org/0000-0003-3119-9385

Kenneth R. Carter − *Conte Center for Polymer Research, Department of Polymer Science and Engineering, University of Massachusetts Amherst, Amherst, Massachusetts 01003, United States*

Guangwen Zhou − *Department of Materials Science and Engineering, Binghamton University, State University of New York at Binghamton, Binghamton, New York 13850, United States;* orcid.org/0000-0002-9243-293X

Peng Bai − *Department of Chemical Engineering, University of Massachusetts Amherst, Amherst, Massachusetts 01003, United States;* orcid.org/0000-0002-6881-4663

Complete contact information is available at: https://pubs.acs.org/10.1021/acsami.3c18693

Author Contributions

†D.S. and H.-J.Y. contributed equally. Dipankar Saha: conceptualization, investigation, data analysis, writing—original draft, writing—review and editing. Hsin-Jung Yu: conceptualization, investigation, data analysis, writing—original draft, writing—review and editing. Jiacheng Wang: theoretical investigation, data analysis, writing—review and editing. Prateek: investigation, writing—review and editing. Xiaobo Chen: HAADF-STEM investigation. Chaoyun Tang: writing—review and editing. Claire Senger: investigation. James Nicolas Pagaduan: writing—review and editing. Reika Katsumata: writing—review and editing. Kenneth R. Carter: investigation. Guangwen Zhou: HAADF-STEM investigation. Peng Bai: conceptualization, funding acquisition, supervision, writing—review and editing. Nianqiang Wu: conceptualization, supervision, writing—review and editing. James J. Watkins: conceptualization, supervision, funding acquisition, writing—review and editing.

Notes

The authors declare no competing financial interest.

■ ACKNOWLEDGMENTS

The authors are grateful to acknowledge the Penn State Materials Characterization Lab for the use of the XPS instrument and Jeffrey Shallenberger for helpful discussions on sample preparation and measurement; Dr. Alexander Ribbe (UMass, Amherst, USA) for high-resolution TEM; the facility services for electronic microscopy, spectroscopy, XRD, and SAXS at the Department of Polymer Science and Engineering, and the Institute of Applied Sciences at the University of Massachusetts, Amherst, USA. The authors are also thankful to the Watkins group members, particularly Takumi Uchiyama and Varun Pande, the Wu group members particularly Yingjie Hang; Dr. Vinay Patel (IIT-Bombay, India), Professor Jayasree Biswas (IIT-Bombay, India), Dr. Munusamy Krishnamurthy (UMass Amherst), and Professor Wei Fan and Dr. Kaivalya Gawande (both from the Chemical Engineering Department, UMass, Amherst, USA) for fruitful discussions. Peng Bai acknowledges the financial support from the National Science Foundation (Grant CBET 2144360). The computer calculations used resources of the National Energy Research Scientific Computing Center (NERSC) through allocation ERCAP0021594 and of the Advanced Cyberinfrastructure Coordination Ecosystem (ACCESS) through allocation CTS190069. James J. Watkins acknowledges financial support from the U.S. Army Research Laboratory (under the National Center for Manufacturing Sciences Award HQ0034-15-2-0007, Expeditionary Maneuver Support Award W911QY1990011), as well as Office of Naval Research (under LIFT Award N000142190010).

■ REFERENCES

(1) Saha, D.; Patel, V.; Selvaganapathy, P. R.; Kruse, P. Facile fabrication of conductive MoS2 thin films by sonication in hot water and evaluation of their electrocatalytic performance in the hydrogen evolution reaction. *Nanoscale Advances* **2021**, *4* (1), 125−137.

(2) Saha, D.; Kruse, P. Editors' Choice—Review—Conductive Forms of MoS2 and Their Applications in Energy Storage and Conversion. *J. Electrochem. Soc.* **2020**, *167* (12), 126517.

(3) Saha, D.; Dalmieda, J.; Patel, V. Surface-Modified MXenes: Simulation to Potential Applications. *ACS Applied Electronic Materials* **2023**, *5* (6), 2933−2955.

(4) Zhou, H.; Yu, F.; Sun, J.; He, R.; Chen, S.; Chu, C.-W.; Ren, Z. Highly active catalyst derived from a 3D foam of Fe(PO3)2/Ni2P for extremely efficient water oxidation. *Proc. Natl. Acad. Sci. U. S. A.* **2017**, *114* (22), 5607−5611.

(5) Gao, S.; Lin, Y.; Jiao, X.; Sun, Y.; Luo, Q.; Zhang, W.; Li, D.; Yang, J.; Xie, Y. Partially oxidized atomic cobalt layers for carbon dioxide electroreduction to liquid fuel. *Nature* **2016**, *529* (7584), 68−71.

(6) Liang, Z.; Lu, Y.-C. Critical Role of Redox Mediator in Suppressing Charging Instabilities of Lithium-Oxygen Batteries. *J. Am. Chem. Soc.* **2016**, *138* (24), 7574−7583.

(7) Walter, M. G.; Warren, E. L.; McKone, J. R.; Boettcher, S. W.; Mi, Q.; Santori, E. A.; Lewis, N. S. Solar Water Splitting Cells. *Chem. Rev.* **2010**, *110* (11), 6446−6473.

(8) Ismail, F.; Abdellah, A.; Sudheeshkumar, V.; Rakhsha, A.; Chen, W.; Chen, N.; Higgins, D. C. Atomically Isolated Nickel-Nitrogen-Carbon Electrocatalysts Derived by the Utilization of Mg2+ ions as Spacers in Bimetallic Ni/Mg-Metal-Organic Framework Precursors for Boosting the Electroreduction of CO2. *ACS Applied Energy Materials* **2022**, *5* (8), 9408−9417.

(9) Kumar, P.; Kannimuthu, K.; Zeraati, A. S.; Roy, S.; Wang, X.; Wang, X.; Samanta, S.; Miller, K. A.; Molina, M.; Trivedi, D.; et al. High-Density Cobalt Single-Atom Catalysts for Enhanced Oxygen Evolution Reaction. *J. Am. Chem. Soc.* **2023**, *145* (14), 8052−8063.

(10) Tang, C.; Ramírez-Hernández, M.; Thomas, B.; Yeh, Y.-W.; Batson, P. E.; Asefa, T. Hierarchically Ordered Nanoporous Carbon with Exclusively Surface-Anchored Cobalt as Efficient Electrocatalyst. *Small Methods* **2022**, *6* (7), 2200519.

(11) Tang, C.; Thomas, B.; Ramírez-Hernández, M.; Mikmeková, E. M.; Asefa, T. Metal-Functionalized Hydrogels as Efficient Oxygen Evolution Electrocatalysts. *ACS Appl. Mater. Interfaces* **2022**, *14* (18), 20919−20929.

(12) Arcelus-Arrillaga, P.; Pinilla, J. L.; Hellgardt, K.; Millan, M. Application of Water in Hydrothermal Conditions for Upgrading Heavy Oils: A Review. *Energy Fuels* **2017**, *31* (5), 4571−4587.

(13) Katsumata, R.; Limary, R.; Zhang, Y.; Popere, B. C.; Heitsch, A. T.; Li, M.; Trefonas, P.; Segalman, R. A. Mussel-Inspired Strategy for Stabilizing Ultrathin Polymer Films and Its Application to Spin-On Doping of Semiconductors. *Chem. Mater.* **2018**, *30* (15), 5285−5292.

(14) Chu, J. H.; Kwak, J.; Kwon, T.-Y.; Park, S.-D.; Go, H.; Kim, S. Y.; Park, K.; Kang, S.; Kwon, S.-Y. Facile Synthesis of Few-Layer Graphene with a Controllable Thickness Using Rapid Thermal Annealing. *ACS Appl. Mater. Interfaces* **2012**, *4* (3), 1777−1782.

(15) Pagaduan, J. N.; Samitsu, S.; Varma, J.; Emrick, T.; Katsumata, R. Freeze-Burn: Fabrication of Porous Carbon Networks via Polymer-Templated Rapid Thermal Annealing. *ACS Applied Polymer Materials* **2022**, *4* (6), 4329−4338.

(16) Bhardwaj, A.; Pagaduan, J. N.; Yu, Y.-G.; Einck, V. J.; Nuguri, S.; Katsumata, R.; Watkins, J. J. Large-Pore Ordered Mesoporous Turbostratic Carbon Films Prepared Using Rapid Thermal Annealing for High-Performance Micro-pseudocapacitors. *ACS Appl. Mater. Interfaces* **2021**, *13* (51), 61027−61038.

(17) Fei, H.-F.; Long, Y.; Yu, H.-J.; Yavitt, B. M.; Fan, W.; Ribbe, A.; Watkins, J. J. Bimodal Mesoporous Carbon Spheres with Small and Ultra-Large Pores Fabricated Using Amphiphilic Brush Block Copolymer Micelle Templates. *ACS Appl. Mater. Interfaces* **2020**, *12* (51), 57322−57329.

(18) Fei, H.-F.; Li, W.; Bhardwaj, A.; Nuguri, S.; Ribbe, A.; Watkins, J. J. Ordered Nanoporous Carbons with Broadly Tunable Pore Size Using Bottlebrush Block Copolymer Templates. *J. Am. Chem. Soc.* **2019**, *141* (42), 17006−17014.
(19) Fei, H.-F.; Li, W.; Nuguri, S.; Yu, H.-J.; Yavitt, B. M.; Fan, W.; Watkins, J. J. One-Step Synthesis of Hierarchical, Bimodal Nanoporous Carbons via Co-templating with Bottlebrush and Linear Block Copolymers. *Chem. Mater.* **2020**, *32* (14), 6055−6061.
(20) Meng, Y.; Wang, S.; Li, C.; Qian, M.; Yan, X.; Yao, S.; Peng, X.; Wang, Y.; Huang, R. Photothermal combined gene therapy achieved by polyethyleneimine-grafted oxidized mesoporous carbon nanospheres. *Biomaterials* **2016**, *100*, 134−142.
(21) Aviv, Y.; Altay, E.; Rzayev, J.; Shenhar, R. Assembly of Bottlebrush Block Copolymers and Nanoparticles in Ultrathin Films: Effect of Substrate-Copolymer Interaction on the Nanocomposite Morphology. *Macromolecules* **2021**, *54* (13), 6247−6256.
(22) Peng, L.; Hung, C.-T.; Wang, S.; Zhang, X.; Zhu, X.; Zhao, Z.; Wang, C.; Tang, Y.; Li, W.; Zhao, D. Versatile Nanoemulsion Assembly Approach to Synthesize Functional Mesoporous Carbon Nanospheres with Tunable Pore Sizes and Architectures. *J. Am. Chem. Soc.* **2019**, *141* (17), 7073−7080.
(23) Lin, Y.; Wang, X.; Qian, G.; Watkins, J. J. Additive-Driven Self-Assembly of Well-Ordered Mesoporous Carbon/Iron Oxide Nanoparticle Composites for Supercapacitors. *Chem. Mater.* **2014**, *26* (6), 2128−2137.
(24) Tirumala, V. R.; Romang, A.; Agarwal, S.; Lin, E. K.; Watkins, J. J. Well Ordered Polymer Melts from Blends of Disordered Triblock Copolymer Surfactants and Functional Homopolymers. *Adv. Mater.* **2008**, *20* (9), 1603−1608.
(25) Tirumala, V. R.; Daga, V.; Bosse, A. W.; Romang, A.; Ilavsky, J.; Lin, E. K.; Watkins, J. J. Well-Ordered Polymer Melts with 5 nm Lamellar Domains from Blends of a Disordered Block Copolymer and a Selectively Associating Homopolymer of Low or High Molar Mass. *Macromolecules* **2008**, *41* (21), 7978−7985.
(26) Lee, S.; Bluemle, M. J.; Bates, F. S. Discovery of a Frank-Kasper σ Phase in Sphere-Forming Block Copolymer Melts. *Science* **2010**, *330* (6002), 349−353.
(27) Xue, J.; Li, Y.; Hu, J. Nanoporous bimetallic Zn/Fe-N-C for efficient oxygen reduction in acidic and alkaline media. *Journal of Materials Chemistry A* **2020**, *8* (15), 7145−7157.
(28) Wan, X.; Liu, Q.; Liu, J.; Liu, S.; Liu, X.; Zheng, L.; Shang, J.; Yu, R.; Shui, J. Iron atom-cluster interactions increase activity and improve durability in Fe-N-C fuel cells. *Nat. Commun.* **2022**, *13* (1), 2963.
(29) Jin, Z.; Li, P.; Meng, Y.; Fang, Z.; Xiao, D.; Yu, G. Understanding the inter-site distance effect in single-atom catalysts for oxygen electroreduction. *Nature Catalysis* **2021**, *4* (7), 615−622.
(30) Angizi, S.; Yu, E. Y. C.; Dalmieda, J.; Saha, D.; Selvaganapathy, P. R.; Kruse, P. Defect Engineering of Graphene to Modulate pH Response of Graphene Devices. *Langmuir* **2021**, *37* (41), 12163−12178.
(31) Yang, G.; Zhu, J.; Yuan, P.; Hu, Y.; Qu, G.; Lu, B.-A.; Xue, X.; Yin, H.; Cheng, W.; Cheng, J.; et al. Regulating Fe-spin state by atomically dispersed Mn-N in Fe-N-C catalysts with high oxygen reduction activity. *Nat. Commun.* **2021**, *12* (1), 1734.
(32) Cursaru, L. M.; Piticescu, R. M.; Dragut, D. V.; Tudor, I. A.; Kuncser, V.; Iacob, N.; Stoiciu, F. The Influence of Synthesis Parameters on Structural and Magnetic Properties of Iron Oxide Nanomaterials. *Nanomaterials* **2020**, *10* (1), 85.
(33) Tan, H.; Tang, J.; Henzie, J.; Li, Y.; Xu, X.; Chen, T.; Wang, Z.; Wang, J.; Ide, Y.; Bando, Y.; et al. Assembly of Hollow Carbon Nanospheres on Graphene Nanosheets and Creation of Iron-Nitrogen-Doped Porous Carbon for Oxygen Reduction. *ACS Nano* **2018**, *12* (6), 5674−5683.
(34) Ngidi, N. P. D.; Ollengo, M. A.; Nyamori, V. O. Effect of Doping Temperatures and Nitrogen Precursors on the Physicochemical, Optical, and Electrical Conductivity Properties of Nitrogen-Doped Reduced Graphene Oxide. *Materials* **2019**, *12* (20), 3376.
(35) Yan, W.; Wang, L.; Chen, C.; Zhang, D.; Li, A.-J.; Yao, Z.; Shi, L.-Y. Polystyrene Microspheres-Templated Nitrogen-Doped Graphene Hollow Spheres as Metal-Free Catalyst for Oxygen Reduction Reaction. *Electrochim. Acta* **2016**, *188*, 230−239.
(36) Chatterjee, R.; Sajjadi, B.; Chen, W.-Y.; Mattern, D. L.; Hammer, N.; Raman, V.; Dorris, A. Effect of Pyrolysis Temperature on PhysicoChemical Properties and Acoustic-Based Amination of Biochar for Efficient CO2 Adsorption. *Front. Energy Res.* **2020**, *8*, 85.
(37) Wang, D.; Xu, Y.; Guo, X.; Fu, Z.; Yang, Z.; Sun, W. Nickel foam as conductive substrate enhanced low-crystallinity two-dimensional iron hydrogen phosphate for oxygen evolution reaction. *J. Alloys Compd.* **2021**, *870*, 159472.
(38) Kundu, A.; Robby, A. I.; Shit, A.; Jo, H. J.; Park, S. Y. Construction of FeCo2O4@N-Doped Carbon Dots Nanoflowers as Binder Free Electrode for Reduction and Oxidation of Water. *Materials* **2020**, *13* (14), 3119.
(39) He, Y.; Liu, S.; Priest, C.; Shi, Q.; Wu, G. Atomically dispersed metal-nitrogen-carbon catalysts for fuel cells: advances in catalyst design, electrode performance, and durability improvement. *Chem. Soc. Rev.* **2020**, *49* (11), 3484−3524.
(40) Fu, H.; Liu, Y.; Chen, L.; Shi, Y.; Kong, W.; Hou, J.; Yu, F.; Wei, T.; Wang, H.; Guo, X. Designed formation of NiCo2O4 with different morphologies self-assembled from nanoparticles for asymmetric supercapacitors and electrocatalysts for oxygen evolution reaction. *Electrochim. Acta* **2019**, *296*, 719−729.
(41) Wang, D.; Xu, Y.; Sun, W.; Guo, X.; Yang, L.; Wang, F.; Yang, Z. Ultrasonic treatment of Co7(PO4)2(HPO4)4 using NMP for supercapacitors and oxygen evolution reaction. *Electrochim. Acta* **2020**, *337*, 135827.
(42) Bai, L.; Hsu, C.-S.; Alexander, D. T. L.; Chen, H. M.; Hu, X. A Cobalt-Iron Double-Atom Catalyst for the Oxygen Evolution Reaction. *J. Am. Chem. Soc.* **2019**, *141* (36), 14190−14199.
(43) Salarizadeh, P.; Askari, M. B.; Seifi, M.; Rozati, S. M. MoS2 coating on different carbonaceous materials: Comparison of electrochemical properties and hydrogen evolution reaction performance. *J. Electroanal. Chem.* **2019**, *847*, 113198.
(44) Li, W.; Zhang, Z.; Zhang, W.; Zou, S. MoS2 Nanosheets Supported on Hollow Carbon Spheres as Efficient Catalysts for Electrochemical Hydrogen Evolution Reaction. *ACS Omega* **2017**, *2* (8), 5087−5094.
(45) Tan, W.; Xie, S.; Yang, J.; Lv, J.; Yin, J.; Zhang, C.; Wang, J.; Shen, X.; Zhao, M.; Zhang, M.; et al. Effect of carbonization temperature on electrocatalytic water splitting of Fe-Co anchored on N-doped porous carbon. *J. Solid State Chem.* **2021**, *302*, 122435.
(46) Connor, P.; Schuch, J.; Kaiser, B.; Jaegermann, W. The Determination of Electrochemical Active Surface Area and Specific Capacity Revisited for the System MnOx as an Oxygen Evolution Catalyst. *Zeitschrift für Physikalische Chemie* **2020**, *234* (5), 979−994 (accessed Apr 23, 2023).
(47) Zheng, M.; Xu, H.; Li, Y.; Ding, K.; Zhang, Y.; Sun, C.; Chen, W.; Lin, W. Electrocatalytic Nitrogen Reduction by Transition Metal Single-Atom Catalysts on Polymeric Carbon Nitride. *J. Phys. Chem. C* **2021**, *125* (25), 13880−13888.
(48) Zhao, Z.; Zhou, W.; Lin, D.; Zhu, L.; Xing, B.; Liu, Z. Construction of dual active sites on diatomic metal (FeCo-N/C-x) catalysts for enhanced Fenton-like catalysis. *Applied Catalysis B: Environmental* **2022**, *309*, 121256.
(49) Shang, R.; Steinmann, S. N.; Xu, B.-Q.; Sautet, P. Mononuclear Fe in N-doped carbon: computational elucidation of active sites for electrochemical oxygen reduction and oxygen evolution reactions. *Catalysis Science & Technology* **2020**, *10* (4), 1006−1014.
(50) de Oliveira, F. T.; Chanda, A.; Banerjee, D.; Shan, X.; Mondal, S.; Que, L.; Bominaar, E. L.; Münck, E.; Collins, T. J. Chemical and Spectroscopic Evidence for an Fe^{V}-Oxo Complex. *Science* **2007**, *315* (5813), 835−838.
(51) Ellis, W. C.; McDaniel, N. D.; Bernhard, S.; Collins, T. J. Fast Water Oxidation Using Iron. *J. Am. Chem. Soc.* **2010**, *132* (32), 10990−10991.

https://doi.org/10.1021/acsami.3c18693
ACS Appl. Mater. Interfaces 2024, 16, 13729−13744

(52) Ertem, M. Z.; Gagliardi, L.; Cramer, C. J. Quantum chemical characterization of the mechanism of an iron-based water oxidation catalyst. *Chemical Science* **2012**, *3* (4), 1293−1299.
(53) Ho, J.; Coote, M. L. A universal approach for continuum solvent pKa calculations: are we there yet? *Theor. Chem. Acc.* **2010**, *125* (1), 3−21.
(54) Marenich, A. V.; Ho, J.; Coote, M. L.; Cramer, C. J.; Truhlar, D. G. Computational electrochemistry: prediction of liquid-phase reduction potentials. *Phys. Chem. Chem. Phys.* **2014**, *16* (29), 15068−15106.
(55) Guerard, J. J.; Arey, J. S. Critical Evaluation of Implicit Solvent Models for Predicting Aqueous Oxidation Potentials of Neutral Organic Compounds. *J. Chem. Theory Comput.* **2013**, *9* (11), 5046−5058.
(56) Wang, Y.; Jin, X.; Yu, H. S.; Truhlar, D. G.; He, X. Revised M06-L functional for improved accuracy on chemical reaction barrier heights, noncovalent interactions, and solid-state physics. *Proc. Natl. Acad. Sci. U. S. A.* **2017**, *114* (32), 8487−8492.
(57) Yuan, K.; Lützenkirchen-Hecht, D.; Li, L.; Shuai, L.; Li, Y.; Cao, R.; Qiu, M.; Zhuang, X.; Leung, M. K. H.; Chen, Y.; et al. Boosting Oxygen Reduction of Single Iron Active Sites via Geometric and Electronic Engineering: Nitrogen and Phosphorus Dual Coordination. *J. Am. Chem. Soc.* **2020**, *142* (5), 2404−2412.
(58) Yu, Y.; Xiao, D.; Ma, J.; Chen, C.; Li, K.; Ma, J.; Liao, Y.; Zheng, L.; Zuo, X. The self-template synthesis of highly efficient hollow structure Fe/N/C electrocatalysts with Fe-N coordination for the oxygen reduction reaction. *RSC Adv.* **2018**, *8* (43), 24509−24516.
(59) Biesinger, M. C. Accessing the robustness of adventitious carbon for charge referencing (correction) purposes in XPS analysis: Insights from a multi-user facility data review. *Appl. Surf. Sci.* **2022**, *597*, 153681.
(60) Gao, L.; Cui, X.; Wang, Z.; Sewell, C. D.; Li, Z.; Liang, S.; Zhang, M.; Li, J.; Hu, Y.; Lin, Z. *Operando* unraveling photothermal-promoted dynamic active-sites generation in $NiFe_2O_4$ for markedly enhanced oxygen evolution. *Proc. Natl. Acad. Sci. U. S. A.* **2021**, *118* (7), No. e2023421118.
(61) Liu, K.; Zhang, C.; Sun, Y.; Zhang, G.; Shen, X.; Zou, F.; Zhang, H.; Wu, Z.; Wegener, E. C.; Taubert, C. J.; et al. High-Performance Transition Metal Phosphide Alloy Catalyst for Oxygen Evolution Reaction. *ACS Nano* **2018**, *12* (1), 158−167.
(62) Peng, L.; Yang, J.; Yang, Y.; Qian, F.; Wang, Q.; Sun-Waterhouse, D.; Shang, L.; Zhang, T.; Waterhouse, G. I. N. Mesopore-Rich Fe-N-C Catalyst with FeN4-O-NC Single-Atom Sites Delivers Remarkable Oxygen Reduction Reaction Performance in Alkaline Media. *Adv. Mater.* **2022**, *34* (29), 2202544.
(63) Krause, S.; Overgaard, M. H.; Vosch, T. Photon Energy Dependent Micro-Raman Spectroscopy with a Continuum Laser Source. *Sci. Rep.* **2018**, *8* (1), 11621.
(64) Zhang, C. C.; Hartlaub, S.; Petrovic, I.; Yilmaz, B. Raman Spectroscopy Characterization of Amorphous Coke Generated in Industrial Processes. *ACS Omega* **2022**, *7* (3), 2565−2570.
(65) Dong, J.; Qian, Z.; Xu, P.; Yue, M.-F.; Zhou, R.-Y.; Wang, Y.; Nan, Z.-A.; Huang, S.; Dong, Q.; Li, J.-F.; et al. In situ Raman spectroscopy reveals the structure evolution and lattice oxygen reaction pathway induced by the crystalline-amorphous hetero-junction for water oxidation. *Chemical Science* **2022**, *13* (19), 5639−5649.
(66) Hedenstedt, K.; Bäckström, J.; Ahlberg, E. In-Situ Raman Spectroscopy of α- and γ-FeOOH during Cathodic Load. *J. Electrochem. Soc.* **2017**, *164* (9), H621.
(67) Jamil, R.; Ali, R.; Loomba, S.; Xian, J.; Yousaf, M.; Khan, K.; Shabbir, B.; McConville, C. F.; Mahmood, A.; Mahmood, N. The role of nitrogen in transition-metal nitrides in electrochemical water splitting. *Chem. Catalysis* **2021**, *1* (4), 802−854.
(68) Chenitz, R.; Kramm, U. I.; Lefèvre, M.; Glibin, V.; Zhang, G.; Sun, S.; Dodelet, J.-P. A specific demetalation of Fe-N4 catalytic sites in the micropores of NC_Ar + NH3 is at the origin of the initial activity loss of the highly active Fe/N/C catalyst used for the reduction of oxygen in PEM fuel cells. *Energy Environ. Sci.* **2018**, *11* (2), 365−382.
(69) Hyatt, M. G.; Walsh, D. J.; Lord, R. L.; Andino Martinez, J. G.; Guironnet, D. Mechanistic and Kinetic Studies of the Ring Opening Metathesis Polymerization of Norbornenyl Monomers by a Grubbs Third Generation Catalyst. *J. Am. Chem. Soc.* **2019**, *141* (44), 17918−17925.
(70) Saha, D.; Selvaganapathy, P. R.; Kruse, P. Peroxide-Induced Tuning of the Conductivity of Nanometer-Thick MoS2 Films for Solid-State Sensors. *ACS Applied Nano Materials* **2020**, *3* (11), 10864−10877.
(71) Frisch, M. J.; et al. *Gaussian 16*, revision C.01; Gaussian, Inc.: Wallingford, CT, 2016.
(72) Zhao, Y.; Truhlar, D. G. A new local density functional for main-group thermochemistry, transition metal bonding, thermochemical kinetics, and noncovalent interactions. *J. Chem. Phys.* **2006**, *125* (19), 194101.
(73) Kendall, R. A.; Dunning, T. H.; Harrison, R. J. Electron affinities of the first-row atoms revisited. Systematic basis sets and wave functions. *J. Chem. Phys.* **1992**, *96* (9), 6796−6806.
(74) Dolg, M.; Wedig, U.; Stoll, H.; Preuss, H. Energy-adjusted ab initio pseudopotentials for the first row transition elements. *J. Chem. Phys.* **1987**, *86* (2), 866−872.
(75) Marenich, A. V.; Cramer, C. J.; Truhlar, D. G. Universal Solvation Model Based on Solute Electron Density and on a Continuum Model of the Solvent Defined by the Bulk Dielectric Constant and Atomic Surface Tensions. *J. Phys. Chem. B* **2009**, *113* (18), 6378−6396.
(76) Kelly, C. P.; Cramer, C. J.; Truhlar, D. G. Single-Ion Solvation Free Energies and the Normal Hydrogen Electrode Potential in Methanol, Acetonitrile, and Dimethyl Sulfoxide. *J. Phys. Chem. B* **2007**, *111* (2), 408−422.

https://doi.org/10.1021/acsami.3c18693
ACS Appl. Mater. Interfaces 2024, 16, 13729−13744